ImmunoTargets and Therapy

Dovepress
Taylor & Francis Group

Open Access Full Text Article

ORIGINAL RESEARCH

Fracture-Induced Immunological Cascades Trigger Rapid Systemic Bone Loss via Osteocyte-Regulated Osteoclastogenesis

Lipeng Sun[1], Shouxiang Kuang[1], Yang Li[1], Guodong Wang[1], Jianmin Sun[1], Fengge Zhou[2,*], Chenggui Zhang[1,*]

[1]Department of Orthopaedics, Shandong Provincial Hospital Affiliated to Shandong First Medical University, Jinan, Shandong, People's Republic of China; [2]Tumor Research and Therapy Center, Shandong Provincial Hospital Affiliated to Shandong First Medical University, Jinan, Shandong, People's Republic of China

*These authors contributed equally to this work

Correspondence: Chenggui Zhang, Department of Orthopaedics, Shandong Provincial Hospital Affiliated to Shandong First Medical University, 9677 Jingshi Road, Jinan, Shandong, 250000, People's Republic of China, Tel +86 531 6877 3207, Email chenggui1214@pku.edu.cn; Fengge Zhou, Email zfg1991125@163.com

Background: Rapid bone loss after fracture elevates the risk of subsequent fractures, but the mechanisms remain unclear. IL-6, a key cytokine involved in fracture healing, is markedly upregulated during the immune response after fracture; however, its role in systemic skeletal deterioration remains poorly defined.

Methods: In this study, we employed label-free proteomics to identify candidate mediators in vertebral samples following fracture. Next, osteocyte siRNA knockdown and Stattic (STAT3 phosphorylation inhibitor) inhibition were used to investigate IL-6 related signaling pathways. Subsequently, indirect co-cultures of osteocyte with osteoclast or osteoblast were used to evaluate the effects of the IL-6 pathway on bone resorption and formation. Furthermore, fractured mice were treated with MR16-1 (monoclonal anti-mouse IL-6 receptor antibody) or Stattic. Then, trabecular and cortical bone in vertebrae and femur were evaluated at 4, 14, and 28 days post-fracture, including histological analysis of p-STAT3$^+$ osteocyte, RANKL expression, and bone formation/resorption markers.

Results: : In vitro, IL-6 dose-dependently elevated RANKL and p-STAT3 levels in osteocyte and promoted osteoclast activity in co-culture. These effects were suppressed by Stattic and replicated by STAT3 knockdown. In contrast, co-culture of osteocyte with osteoblast exhibited no significant alterations in osteogenic marker expression upon IL-6 exposure, suggesting negligible effects on osteoblast activity. In vivo, MR16-1 reduced trabecular bone loss in the vertebrae and femur after fracture. It also diminished p-STAT3$^+$ osteocyte, reduced RANKL expression, and suppressed osteoclast activity without impairing osteoblastogenesis. And Stattic produced a comparable reduction in systemic bone loss and osteoclast overactivation.

Conclusion: This study demonstrates that IL-6 drives osteoclast-mediated bone resorption via STAT3-dependent RANKL induction in osteocyte, thereby aggravating post-fracture systemic bone loss. And the findings highlight that modulating the IL-6/STAT3/RANKL axis and targeting osteocyte function may offer a promising therapeutic approach for preventing bone loss and minimizing the risk of fracture recurrence.

Keywords: osteoporosis, fracture healing, fracture risk, osteocyte, RANKL, inflammation

Introduction

The rapid increase in the risk of refracture shortly after an initial fracture, known as imminent fracture risk, is a critical concern.[1–5] Our study and previous early studies identified systemic bone loss after fracture as a significant contributor to this increased risk,[6,7] which may perpetuate a vicious cycle of fracture-systemic bone loss-refracture. Research has indicated that the extent of systemic bone loss correlates with age,[7] sex,[8] the severity of the initial fracture,[6] and the skeletal location of bone loss.[9] However, the specific mechanisms underlying bone loss after fracture remain unclear.

Received: 10 April 2025
Accepted: 9 August 2025
Published: 21 August 2025

Inflammation plays an important role in bone loss, including postmenopausal osteoporosis[10–12] and osteoarthritis-associated bone loss.[13–15] Coincidentally, fracture healing can be divided into four phases, with the initial inflammatory phase being a crucial stage.[16] Previous researchers have reported that excessive inflammatory response is detrimental to bone.[17–19] Additionally, clinical trials have demonstrated that targeting inflammation, including the use of IL-6 inhibitors or IL-6 receptor antibodies such as tocilizumab (TCZ), holds therapeutic potential for conditions like osteoarthritis and polymyalgia rheumatica (PMR).[20–23] Now, the rapid advancement in novel drug delivery materials offers innovative strategies for the targeted delivery of IL-6 therapeutics, holding substantial promise for applications in the treatment of associated diseases.[24–26]

Furthermore, as a major molecule that regulates various systems in the body, such as heart health,[27,28] obesity,[29] cancer,[30] autoimmune disease[31] and diabetes,[32] the inflammatory cytokine IL-6, which is released most extensively and at the highest levels during the inflammatory phase, has been associated with various types of osteoporosis.[33–39] Whether the sharp increase in IL-6 during the early inflammatory phase of fracture healing, as reported in previous studies and our studies,[6,40–42] contributes to rapid systemic bone loss during fracture healing remains unknown. Additionally, the specific bone cell type targeted by IL-6 to regulate bone loss remains unclear. However, prior studies have explored the role of IL-6 in osteoclast and osteoblast.[34,43–47] Research has reported both the enhancing[48,49] and inhibitory effects[50,51] of IL-6 on osteoblast, but consensus remains elusive.[52,53] For osteoclast, further investigations suggest that IL-6 may not directly increase osteoclast activity[54,55] but instead requires osteoblast to indirectly promote RANKL, thereby increasing osteoclastic ability.[56,57] Combined with our previous findings that bone loss after fracture has no significant effect on osteoblast and considering the increase in osteoclast activity after fracture,[6] IL-6 may not directly participate in osteoclastic and osteoblastic functions.

Osteocyte, which constitute more than 90–95% of all bone cells and can communicate rapidly,[58,59] play a crucial role in bone metabolism.[60–62] They influence various types of bone loss and participate in the crosstalk of other organs with bone,[63] which highlights their systemic importance.[48,64] The osteocyte-osteoclast axis is well established to enhance osteoclastic activity mediated by RANKL-induced bone loss.[65] We further investigated whether IL-6 can indirectly influence osteoclastic activity through osteocyte, leading to systemic bone loss after fracture.

STAT3 phosphorylation occurs downstream of IL-6 and has recently been discovered to closely regulate various pathways of bone metabolism, which leads to bone loss. Therefore, elucidating the role of the IL-6/ STAT3 phosphorylation pathway in regulating osteocyte would be highly beneficial for uncovering the mechanisms of bone loss after fracture.[66–68] In this study, we aimed to define the role of IL-6 in post-fracture bone loss and further delineate the mechanistic pathways through which IL-6 drives osteocyte-mediated osteoclastic bone resorption.

Materials and Methods

Experimental Design

A total of 102 C57BL/6J male mice, aged 12 weeks, were employed in this research. Male mice were chosen to eliminate the influence of estrogen on bone metabolism, in accordance with previous studies.[6,69,70] These mice were maintained under specific pathogen-free (SPF) conditions with a stable 12-hour light-dark cycle and had unrestricted access to both food and water. After a one-week adaptation phase, 57 mice were randomly distributed into three experimental groups, each comprising 19 individuals (The sample size in this study was determined based on the consistency of intergroup results observed in preliminary experiments and ethical considerations to minimize animal use, in accordance with previous studies).[71,72]

The groups received distinct treatments: femoral fracture group, femoral fracture + MR16-1 group, and control group. To ensure effective blockade of the IL-6 receptor, we selected MR16-1 dosing (0.5 mg per animal, three times per week) as reported in previous literature.[73]

Additionally, a separate animal experiment was conducted using another 45 mice. The mice were further divided into three groups: femoral fracture group, femoral fracture + STAT3 phosphorylation inhibitor (Stattic) group, and control group. Given that previous studies employed Stattic at doses of 10 mg/kg (three times per week)[74] and 20 mg/kg (daily).[75,76] We selected an intermediate dose of 15 mg/kg, administered three times per week, to effectively inhibit STAT3 phosphorylation while minimizing potential toxicity in mice.

Micro-computed tomography (μCT) imaging was conducted on the L5 vertebral body and the contralateral femur at post-fracture 4, 14, and 28 days to evaluate bone microstructure. Additionally, tartrate-resistant acid phosphatase (TRAP) staining was performed on the L5 vertebral body at the same time points to determine osteoclast activity. Sequential fluorescence labeling of the L5 vertebral body was used to investigate bone formation activity. To assess the number of P-STAT3-positive osteocyte and the expression level of RANKL, immunohistochemical analysis was performed. Blood samples were obtained at days 4, 14, and 28 post-fracture to examine systemic inflammatory responses (Figure 1).

All experimental procedures followed ethical guidelines and were approved by the Experimental Animal Ethics Committee of Shandong Provincial Hospital Affiliated to Shandong First Medical University (Approval No. 2022–811).

Label-Free Proteomics

Label-free protein sequencing was performed using four vertebrae derived from two fractured mice and two non-fractured mice, respectively. The specific experimental procedure and data analysis are as follows:

Total Protein Extraction

Frozen tissue samples were placed on ice, and an appropriate volume of lysis buffer (8 M urea, 1% SDS) containing protease inhibitors was added to prevent protein degradation. The mixture was then sonicated for 2 minutes at low temperature, followed by lysis for 30 minutes. Subsequently, the samples were centrifuged at 12,000g at 4°C for 30 minutes. The protein concentration in the supernatant was determined using the Bicinchoninic Acid (BCA) assay following the manufacturer's protocol (Pierce, Thermo, USA).

Protein Reduction, Alkylation, and Digestion

A total of 100 μg of protein was mixed with Triethylammonium Bicarbonate (TEAB) buffer to a final concentration of 100 mM. Tris(2-carboxyethyl)phosphine (TCEP) was then added to a final concentration of 10 mM, followed by incubation at 37°C for 60 minutes. Iodoacetamide (IAM) was subsequently introduced to a final concentration of 40 mM and incubated for 40 minutes at room temperature in the dark. To precipitate proteins, pre-chilled acetone (sample: acetone, v/v = 1:6) was added, and the mixture was incubated at −20 °C for 4 hours. After centrifugation at 10,000g for 20 minutes, the precipitate was collected and resuspended in 100 μL of 100 mM TEAB. Finally, trypsin digestion was performed overnight at 37 °C using a trypsin-to-protein mass ratio of 1:50.

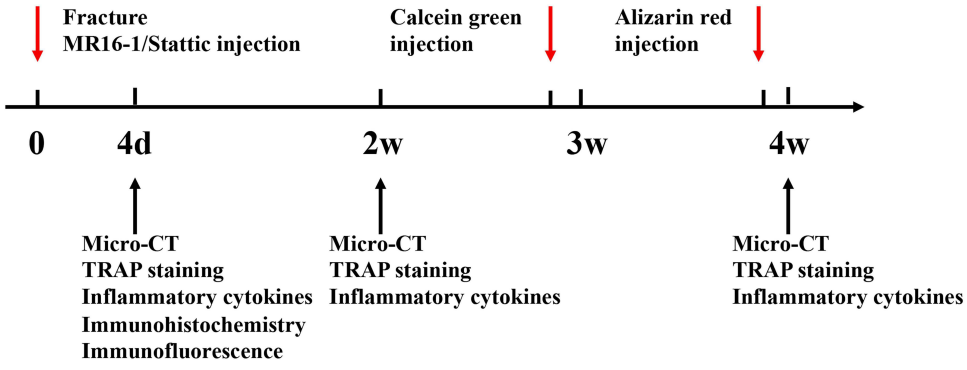

Figure 1 Animal treatment protocol.The initial red arrow indicates that fracture surgery was performed on day 0, followed immediately by the first MR16-1 or Stattic injection. The second red arrow represents the administration of Sequential fluorescence labeling, including calcein green and alizarin red, for dynamic bone formation assessment. Black arrows denote time points for sample collection and analyses, including micro-CT, TRAP staining, inflammatory cytokine quantification, immunohistochemistry, and immunofluorescence. These evaluations were conducted at days 4, 14, and 28 post-fracture.
Abbreviations: TRAP, tartrate-resistant acid phosphatase.

https://doi.org/10.2147/ITT.S533552

Peptide Desalting and Quantification

After vacuum drying, peptides were resuspended in 0.1% trifluoroacetic acid (TFA), desalted using Oasis HLB cartridges, and vacuum dried again. Peptide concentrations were measured using a peptide quantification kit (Thermo, Cat. 23275). Prior to mass spectrometry analysis, loading buffer was added to each sample to achieve a final concentration of 0.25 μg/μL.

LC-MS/MS Analysis

Trypsin-digested peptides were analyzed using an EASY-nLC 1200 system (Thermo, USA) coupled to a Q Exactive HF-X quadrupole Orbitrap mass spectrometer (Thermo, USA) at Majorbio Bio-Pharm Technology Co. Ltd. (Shanghai, China). Chromatographic separation was performed on a C18-reversed phase column (75μm*25 cm, Thermo, USA), equilibrated with solvent A (2% acetonitrile with 0.1% formic acid) and solvent B (80% acetonitrile with 0.1% formic acid). Peptides were eluted using a gradient program: 5%-23% B (0–56 min), 23%-29% B (56–62 min), 29%-38% B (62–63 min), 38%-48% B (63–63.5 min), 48%-100% B (63.5–64 min), and 100% B (64–90 min). Separation was achieved at a flow rate of 300 nL/min.

The Q Exactive HF-X operated in data-dependent acquisition (DDA) mode, alternating between full-scan MS and MS/MS. Full MS scans (m/z 300–1500) were acquired in the Orbitrap at a resolution of 60,000. The automatic gain control (AGC) target was set to 3e6 with a maximum injection time of 20 ms. The top 20 most intense precursor ions were fragmented via higher-energy collision dissociation (HCD). MS/MS spectra were acquired at a resolution of 15,000 (m/z 100), with an AGC target of 1e5, a maximum fill time of 50 ms, and a dynamic exclusion duration of 18 seconds.

Protein Identification

MS/MS spectra were analyzed using Proteome Discoverer 2.4 software. Protein identification was based on the highest-scoring peptide mass match in the database. The search parameters included trypsin digestion with up to two missed cleavages, carbamidomethylation of cysteine residues as a fixed modification, and methionine oxidation and N-terminal acetylation as variable modifications. The false discovery rate (FDR) for peptide identification was set to ≤0.01. A minimum of one unique peptide was required for protein identification.

Statistical Analyses

Proteomic data analysis was performed using the Majorbio Cloud platform (https://cloud.majorbio.com). Differentially expressed proteins (DEPs) between groups were identified using the R package *t*-test,with a significance threshold set at $P < 0.05$ and fold change (FC) >1.2 or <0.83. Functional annotation of identified proteins was conducted using Gene Ontology (GO) (http://geneontology.org/) and Kyoto Encyclopedia of Genes and Genomes (KEGG) pathway analysis (http://www.genome.jp/kegg/). Enrichment analysis of DEPs for GO and KEGG pathways was also performed. Protein-protein interaction (PPI) networks were analyzed using the STRING v11.5 database.

Femoral Fracture

The femoral fracture model in mice was established based on published articles and our previous studies.[6,77] Briefly, mice were anesthetized, and the tibial plateau and femoral condyle were exposed under sterile conditions. A mid-diaphyseal femoral fracture was created using a surgical blade. The fracture site was continuously irrigated with cold saline, and the surrounding muscle was protected from damage. Intramedullary fixation was performed using a 25-gauge syringe needle. Finally, the muscles and skin were sutured with 5/0 silk. All femoral fractures were successfully created, with uncomplicated postoperative recovery observed in all cases. No signs of infection or complications were detected.

Micro Computed Tomography (μCT) Analysis

Micro computed tomography (μ CT) imaging was performed using an Inveon Multi-Modality system (viva CT 40, Scanco Medical, Switzerland) to evaluate the microstructural characteristics of the L5 vertebral body and contralateral

femur. The scans were acquired with an effective voxel size of 10.5 μm, operating at 98 μA current, 100 keV voltage, and an exposure time of 1500 ms per step over 360 rotational increments.

For trabecular bone analysis in the distal femoral metaphysis, measurements were initiated from the metaphyseal growth plate and extended distally over 100 slices. In the L5 vertebral body, the analysis covered the region between the cranial and caudal growth plates. Key trabecular bone parameters, including bone volume fraction (BV/TV), trabecular thickness (Tb.Th), trabecular number (Tb.N), and trabecular separation (Tb.Sp), were automatically quantified.

Cortical bone assessment was conducted at the femoral mid-diaphysis. The region of interest encompassed 120 slices (equivalent to 720 μm) centered at the bone's longitudinal midpoint. Parameters such as cortical bone area (Ct.Ar), total cross-sectional area (Tt.Ar), medullary area (Ma.Ar), cortical thickness (Cort.Th), and the cortical area-to-total cross-sectional area ratio (Ct.Ar/Tt.Ar) were measured.

Enzyme-Linked Immunosorbent Assay (ELISA)

The levels of IL-6, TNF-α and IL-1β serum were measured using commercially available immunoassay kits, following the manufacturer's protocol (IL-6, KYY-0163M1, China; TNF-α, KYY-0132M1, China; IL-1β, KYY-0040M1, China).

TRAP Staining of L5 Vertebral Body

The L5 vertebral body was initially preserved in 4% paraformaldehyde for 24 hours. It was then subjected to decalcification in 10% EDTA at room temperature for 30 days. After completing the decalcification process, the samples were embedded longitudinally in paraffin. Thin sections, each measuring 5 μm in thickness, were prepared and stained using the TRAP staining system (Sigma-Aldrich, St. Louis, MO, USA) following the manufacturer's guidelines.

The quantification of osteoclast was conducted using Image-Pro Plus 6.0 software (Media Cybernetics, Rockville, MD, USA), which measured both the number of osteoclast per bone surface and the osteoclast surface area relative to the bone surface.

Immunohistochemical Staining and Immunofluorescence Labelling

The vertebrae and fractured femurs were initially fixed in 4% paraformaldehyde overnight, followed by decalcification in 10% EDTA and subsequent paraffin embedding using standard procedures. Bone sections, each 5 μm thick, were prepared for immunohistochemical and immunofluorescence analysis. Immunohistochemistry was performed using antibodies targeting RANKL (Bs-0747R; BIOSS; 1:200) and P- STAT3 (GB150001; Servicebio; 1:200), while immunofluorescence staining utilized antibodies against OCN (GB11233; Servicebio; 1:200), IL-6 (GB11117; Servicebio; 1:300), and CTSK (GB111276; Servicebio; 1:500), all following the respective manufacturer's protocols.

After staining, the sections were examined under a Nikon E800 microscope following diaminobenzidine (DAB) substrate treatment. The proportion of osteocyte positively expressing P-STAT3 within the vertebral cancellous bone (500 μm from the growth plate, covering an area of approximately 4 mm^2) was quantified. And the optical density (OD) value of RANKL expression within the same region were measured. Negative control was included for osteocyte density assessment. Quantitative analysis was performed using ImageJ software (version 1.52, NIH, USA). For fluorescently stained tissue sections, the mean fluorescence intensity of Cathepsin K (CTSK) and osteocalcin (OCN) was quantified for each selected non-consecutive section.

Sequential Fluorescence Labelling

To evaluate new bone formation and remodeling, sequential fluorescence labeling was performed. Calcein green (20 mg/kg, Sigma-Aldrich) and Alizarin red (30 mg/kg, Sigma-Aldrich) were administered via tail vein injection 14 days and 7 days before euthanasia, respectively. The L5 vertebral bodies from each group were then fixed in 10% formalin for two weeks, followed by dehydration in a graded ethanol series under vacuum for 48 hours. Subsequently, the specimens were embedded in methyl methacrylate resin.

Undecalcified sections were processed by grinding and polishing to a final thickness of 40–60 μm to obtain longitudinal views of the vertebral body (HistoCore AUTOCUT, Leica Biosystems, Wetzlar, Germany). The mineral apposition rate (MAR) was determined using BioQuant software (BIOQUANT Image Analysis Corporation, Nashville,

TN, USA) by measuring the average distance between the two fluorescent labels and dividing it by the time interval between injections. Additionally, the bone formation rate per bone surface (BFR/BS) and the mineralizing surface relative to the bone surface (MS/BS) were calculated.

Cell Cultures

The murine osteocytic MLO-Y4 cell line (University of Missouri, Kansas City, KS) was used with approval from the Institutional Research Ethics Committee of Shandong Provincial Hospital Affiliated to Shandong First Medical University. No contamination or phenotypic alterations were observed.

The MC3T3-E1 osteoblastic cell line was obtained from Procell Life Science & Technology Co., Ltd. (Wuhan, China) and cultured in α-MEM (Gibco, USA) supplemented with 10% FBS and 1% penicillin-streptomycin at 37°C in a humidified atmosphere containing 5% CO_2. The culture medium was refreshed every two days.

Isolation of Bone Marrow Cells

Twelve-week-old C57BL/6 mice were euthanized and immersed in 75% ethanol for 10 minutes. Femurs and tibias were aseptically isolated under sterile conditions and transferred to PBS. Bone marrow was flushed with α-MEM (Gibco, USA) until the bones turned white. The cell suspension was gently mixed, filtered through a 100 μm strainer, and centrifuged at 1200 rpm for 5 minutes. After discarding the supernatant, red blood cell lysis buffer (Solarbio, China) was added, and the sample was incubated on ice for 10 minutes. Cells were incubated at 37°C with 5% CO_2 overnight. Non-adherent cells were collected, resuspended in α-MEM containing 30 ng/mL M-CSF (BioLegend, USA) and 10% FBS, and incubated for 48 hours. Adherent cells were identified as bone marrow cells (BMMs).

Cell Transfection

MLO-Y4 cells were cultured on rat tail type I collagen-coated plates in α-MEM supplemented with 2.5% FBS, 2.5% calf serum, and 1% penicillin/streptomycin. And cells were seeded in 6-well plates and transfected with control siRNA or STAT3-specific siRNA (siSTAT3; RiboBio, China) using Lipofectamine 2000 transfection reagent (KYY-R Transfection Reagent, China) according to the manufacturer's instructions.[78,79] After 48 hours, cells were treated with recombinant IL-6 for an additional 24 hours to assess downstream effects.

Indirect Coculture System

Osteocyte was seeded on collagen-coated glass plates in α-MEM with 10% FBS and 1% penicillin-streptomycin and incubated for 24 hours. To generate conditioned medium, MLO-Y4 cells were treated with 0, 10, or 50 ng/mL recombinant mouse IL-6 for 24 hours. In parallel, 5 μM Stattic (a small-molecule inhibitor that effectively blocks the activation, transcription, and DNA-binding functions of STAT3) was added to the 50 ng/mL IL-6group and incubated for an additional 6 hours. The dose of Stattic (5 μM) was selected according to published studies.[80] The control group did not receive Stattic.

Conditioned medium was collected and centrifuged, then mixed 1:1 with fresh BMM medium (containing 10% FBS and 1% penicillin/streptomycin). To induce osteoclast formation, mouse BMMs (8000 cells/well) were seeded in 96-well plates and cultured for 2 days in medium with 30 ng/mL M-CSF and 20 ng/mL Recombinant Mouse RANKL. The medium was then replaced with conditioned medium supplemented with 30 ng/mL M-CSF and 30 ng/mL RANKL (R&D Systems, Minneapolis, MN, USA) for indirect coculture. Medium were refreshed every two days, and TRAP staining was performed on day 7.

Then the conditioned medium (CM) from osteocyte was mixed 1:1 with osteogenic induction medium (Gibco, USA) and applied to MC3T3-E1 cells in an indirect coculture system to assess whether IL-6-treated osteocyte CM influences osteoblast activity.

TRAP Staining in Vitro

Following 30-min immobilization in 4% paraformaldehyde solution, cellular specimens underwent dual PBS rinses. Subsequently, samples were incubated with tartrate-resistant acid phosphatase (TRAP) staining solution (Sigma-Aldrich,

St. Louis, MO, USA) under light-protected conditions for 50 min, followed by aqueous washing. Hematoxylin counterstaining was performed for 5 min, with subsequent 10 min bluing treatment using municipal water. After natural drying, cellular morphology was documented through an inverted microscope (Olympus IX53, Tokyo, Japan). In our analyses, mature osteoclasts were identified as TRAP-positive multinucleated cells (≥3 nuclei) directly contact with the bone surface.[44,65] Pre-osteoclast, including TRAP-positive mononuclear cells, were excluded from the quantification. Quantitative analysis of osteoclast surface area was conducted employing ImageJ software (version 1.53t, NIH, USA).

Western Blot Analysis

Protein lysates from primary osteocyte, osteoclast and osteoblast were analyzed by Western blotting. Cells were washed with cold PBS and lysed in RIPA buffer (Shanghai Epizyme Biomedical, China) containing phosphatase and protease inhibitors. Protein concentrations were measured using a BCA assay kit (Beyotime).

Equal amounts of protein were separated by SDS-PAGE, transferred to PVDF membranes (Millipore, USA), and blocked with 5% milk for 1.5 hours. Membranes were incubated overnight at 4°C with primary antibodies against p-STAT3 (CST, 9145T; 1:1000), RANKL (Proteintech, 23408-1-AP; 1:1000), β-actin (Proteintech, 66009–1; 1:20,000), GAPDH (Proteintech, 10494-1-AP,1:5000), NFATC1 (Proteintech, 66963–1; 1:5000), STAT3 (Abcam, ab68153; 1:1000), ALP (Proteintech,18507–1;1:1000), RUNX2 (Proteintech,82636–2;1:2000), and OCN (Wuhan, China; A6205; 1:1000) and CTSK (Wuhan, A1782; 1:300), followed by HRP-conjugated secondary antibodies (Boster, BA1056; 1:5000). Protein bands were visualized using enhanced chemiluminescence (ECL) and quantified with ImageJ software (NIH, Bethesda, MD), with target protein levels normalized to β-actin or GAPDH.

Cellular Immunofluorescence Staining

MLO-Y4 cells (10,000 cells per well) were seeded in 24-well plates, fixed using 4% paraformaldehyde (PFA) and 0.5% Triton X-100 to enhance membrane permeability at room temperature, and then rinsed with PBS. The samples were blocked with 5% bovine serum albumin (BSA) at room temperature, followed by overnight incubation with primary antibodies against p-STAT3 (Cell Signaling Technology, 9145 T; 1:200) and RANKL (Proteintech, 66610–1; 1:400). After the primary antibody incubation, the cells were exposed to secondary fluorescent antibodies in the dark for 1 hour. Following three PBS washes and a 10-minute incubation with DAPI, images were captured using a confocal microscope (Leica, Germany).

Statistical Analysis

Data are presented as mean ± standard deviation (SD), with all individual data points displayed in bar graphs. Statistical analyses were performed using GraphPad Prism 8.0 (GraphPad Software, San Diego, CA, USA). One-way analysis of variance (ANOVA) followed by Tukey's post hoc test or unpaired Student's *t*-test were used for comparisons among groups. A p-value < 0.05 was considered statistically significant. "***" indicates $p < 0.001$ for pathway enrichment significance.

Results

IL-6 Is Regionally and Systemically Upregulated After Femur Fracture and Can Be Neutralized by MR16-1

The label-free proteomics-based KEGG enrichment analysis of the vertebrae from fracture and control group revealed that the different proteins were enriched primarily in inflammatory pathways. Additionally, IL-6 was identified as a key differentially expressed protein (Figure 2A and B).

Immunofluorescence revealed increased IL-6 expression at the femoral fracture site on 4 days after injury, which was significantly reduced in the fracture + MR16-1 group compared to control (Figure 2C).

Furthermore, serum IL-6 levels were significantly elevated in fracture group at 4 days, 2 weeks, and 4 weeks post-injury. Although no difference was observed at day 4, the fracture + MR16-1 group showed a marked reduction in IL-6 levels at 2 and 4 weeks compared to the fracture group (Figure 2D). Serum TNF-α and IL-1β levels were markedly

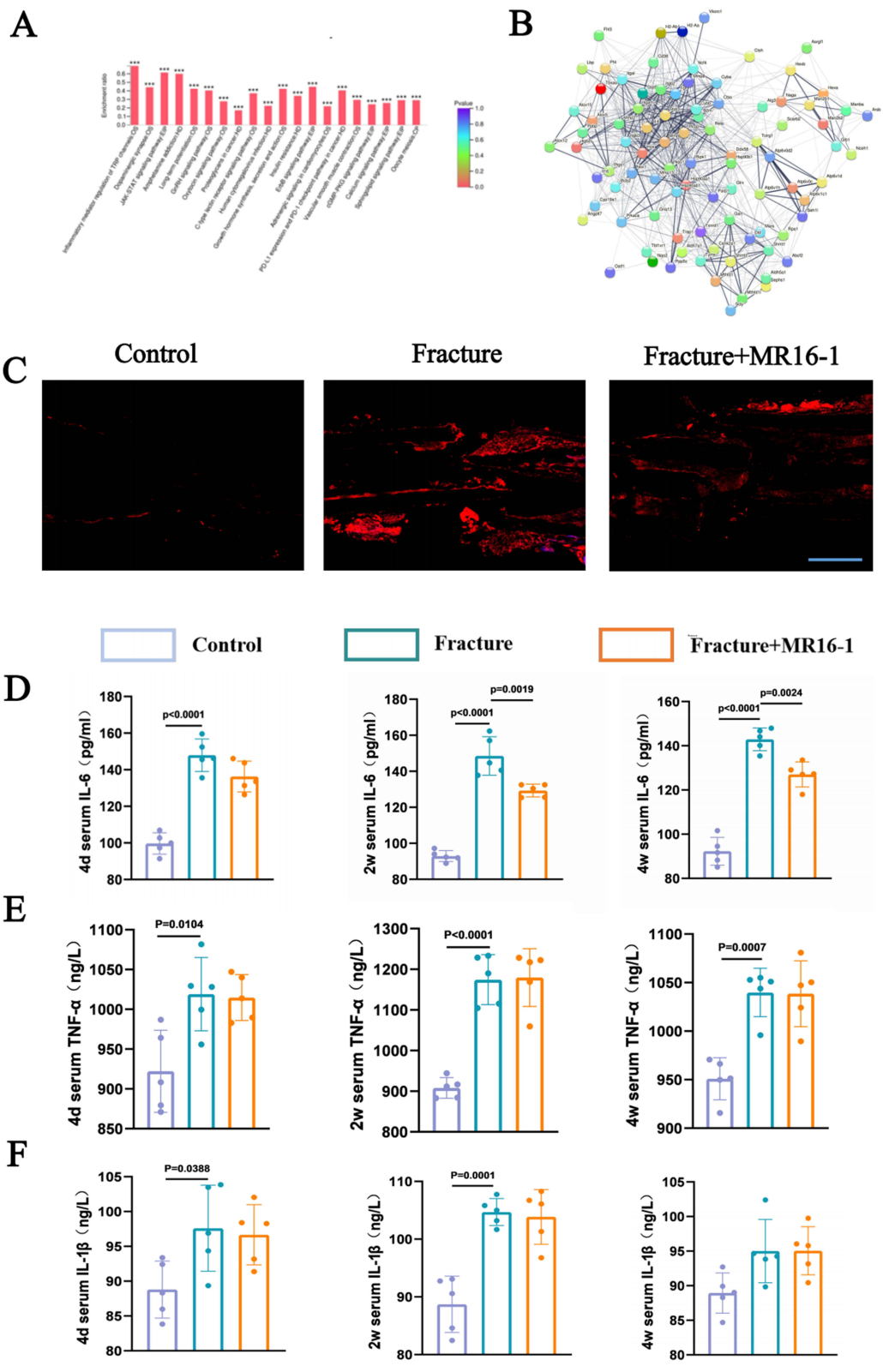

Figure 2 IL-6 levels rapidly increase both locally and systemically after femur fracture, and the use of MR16-1 blocks this increase. (**A**) KEGG enrichment analysis. Differentially expressed proteins were defined by *t*-test ($p < 0.05$, fold change >1.2 or <0.83); "***" indicates $p < 0.001$ for pathway enrichment significance. (n = 2 mice/group). (**B**) Protein interaction analysis. (**C**) Representative images showing the localization of IL-6 fluorescence at the fracture sites in three groups: saline-injected mice, MR16-1-injected mice, and control mice. The scale bar represents 250μm. (**D**) Serum IL-6 levels measured at 4 days, 2 weeks, and 4 weeks after fracture in mice treated with saline, MR16-1, and control (n = 5 mice/group). (**E**) Serum TNF-α levels measured at 4 days, 2 weeks, and 4 weeks after fracture in mice treated with saline, MR16-1, and control (n = 5 mice/group). (**F**) Serum IL-1β levels measured at 4 days, 2 weeks, and 4 weeks after fracture in mice treated with saline, MR16-1, and control (n = 5 mice/group). Error bars indicate standard deviations (SDs). p-values were calculated using one-way ANOVA followed by Tukey's post hoc test.

elevated at 4 days, 2 weeks, and 4 weeks after fracture; however, MR16-1 treatment did not significantly alter these cytokines levels compared to the untreated group (Figure 2E and F).

Systemic Blockade of IL-6 by MR16-1 Reverses Bone Loss After Fracture

Representative 3D images of L5 trabecular bone microarchitecture were obtained at 4 days, 2 weeks, and 4 weeks post-injury for three groups: control, fracture + saline group and fracture + MR16-1 group (Figure 3A–I). Quantitative micro-CT analysis demonstrated that femur fracture led to a significant decrease in trabecular bone volume within the L5 vertebral body at all examined time points (4 days, 2 weeks, and 4 weeks). Nevertheless, administration of MR16-1 markedly enhanced bone structural parameters. At 4 days after femur fracture, the BV/TV of lumbar cancellous bone was significantly lower in fracture + saline group than control. Treatment with MR16-1 significantly increased BV/TV compared to fracture + saline group and showed elevated levels compared to control. Other parameters, including Tb.Th, Tb.N, and Tb.Sp, showed no significant differences among the three groups. (Figure 3J–M). At 2 weeks post-femur fracture, BV/TV and Tb.Th were significantly reduced compared to control. MR16-1 treatment restored these parameters to levels comparable with the saline group. (Figure 3N–Q). Four weeks after femur fracture, BV/TV and Tb.Th decreased significantly, while Tb.Sp increased compared to control. MR16-1 treatment reversed these changes, with no significant differences from control. (Figure 3R–U).

For the contralateral femur diaphysis (Figure 4A–I), BV/TV at 4 days post-fracture was significantly higher in the fracture + MR16-1 group than in the fracture + saline group. (Figure 4J–M). By 2 weeks after fracture, both BV/TV and Tb.N showed a significant decline, Conversely, Tb.Sp was significantly elevated. However, BV/TV in the fracture + MR16-1 group remained significantly higher than that in the fracture + saline group and showed no significant difference from the control group. (Figure 4N–Q). At 4 weeks post-fracture, only BV/TV was significantly lower in fracture + saline group compared to control. MR16-1 treatment significantly increased BV/TV, with no other significant differences observed. (Figure 4R–U).

Cortical bone assessments of the contralateral femur at 4 days, 2 weeks, and 4 weeks post-fracture showed no significant differences among groups (Figure 5A–I). These parameters included cortical thickness (Cort.Th), total tissue area (Tt.Ar), cortical bone area (Ct.Ar), the ratio of cortical area to total area (Ct.Ar/Tr.Ar), and medullary area (Ma.Ar) (Figure 5J–X).

Osteoclast Activity Increases Rapidly and Dramatically After Fracture and Can Be Decreased by MR16-1

TRAP-stained images of the L5 vertebral body are shown for control, saline treated fracture, and MR16-1 treated fracture groups at 4 days (Figure 6A–C), 2 weeks (Figure 6D–F), and 4 weeks post-fracture (Figure 6G–I). At day 4 post-fracture, the saline treated fracture group showed significantly increased osteoclast numbers and surface resorption in L5 trabecular bone compared to control. These increases were markedly reduced in the fracture + MR16-1 group. (Figure 6J and K) Two and four weeks after fracture, osteoclast numbers and surface resorption per bone surface showed no significant differences among the three groups (Figure 6L and O).

Representative CTSK stained images of L5 trabecular bone at 4 days post-fracture were shown for MR16-1 or saline treated group. (Figure 7A) Four days after fracture, CTSK expression, a marker of osteoclast activity, was significantly upregulated in fractured mice, but was effectively suppressed by MR16-1 treatment (Figure 7B).

Osteoblast Activity Remained Stable Following Fracture and Was Not Modulated by MR16-1 or Stattic

At 4 days post-fracture, osteocalcin expression in the L5 trabecular bone was evaluated by immunofluorescence in the control group, the fracture + saline group, and the fracture + MR16-1 group. No significant differences in osteocalcin expression were observed, and MR16-1 did not alter its levels. (Figure 7C and D).

To further evaluate the effects of STAT3 phosphorylation inhibition on osteoclast and osteoblast activity, immunofluorescence staining for CTSK and OCN was performed in L5 vertebrae at 4 days post-fracture. The results showed that

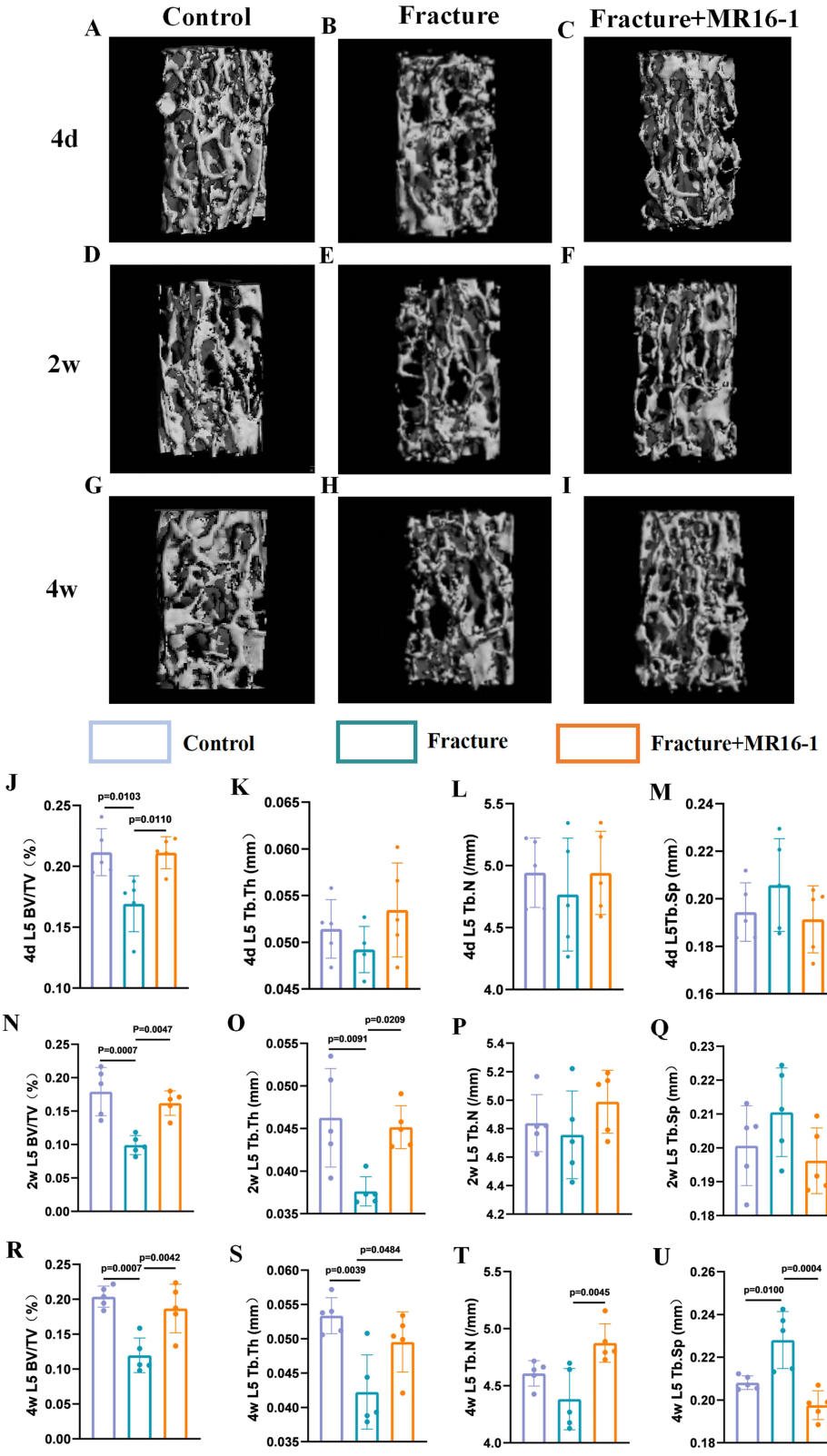

Figure 3 Rapid cancellous bone loss in the L5 vertebra occurs after femur fracture, and the use of MR16-1 alleviates bone loss.(**A–I**) Representative images of the 3D trabecular structure in the L5 vertebral body at 4 days, 2 weeks, and 4 weeks post-fracture in mice treated with saline, MR16-1, or the control group. (**J–U**) Quantitative analysis of trabecular microarchitecture changes in the L5 vertebral body at 4 days, 2 weeks, and 4 weeks post-fracture in mice treated with saline, MR16-1, or control (n = 5 per group). Error bars indicate standard deviations (SDs). p-values were calculated using one-way ANOVA followed by Tukey's post hoc test.
Abbreviations: BV/TV, bone volume/tissue volume; Tb.Th, trabecular thickness; Tb.N, trabecular number; Tb.Sp, trabecular separation.

https://doi.org/10.2147/ITT.S533552

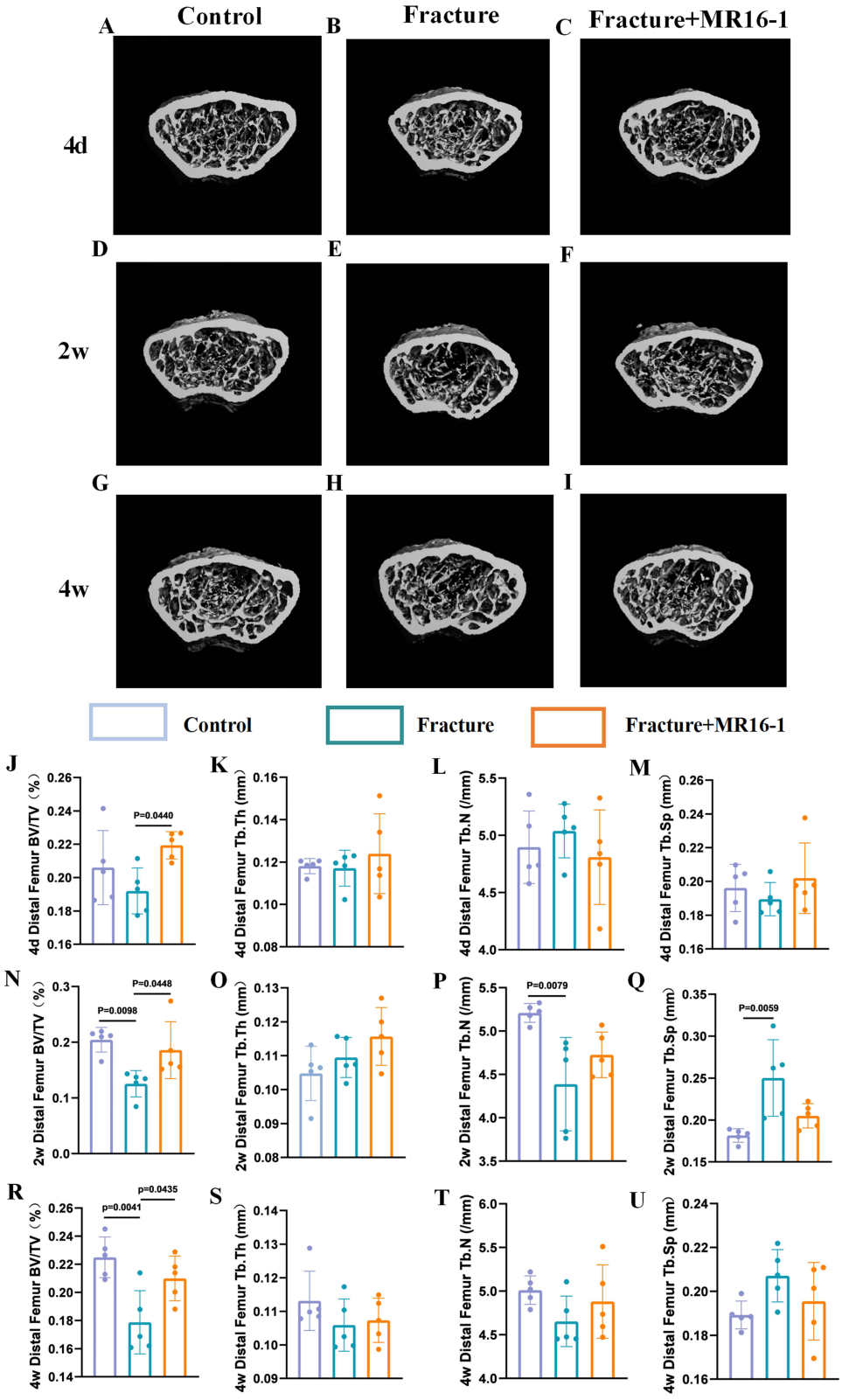

Figure 4 Fracture leads to bone loss in the contralateral distal femur metaphasis, and the use of MR16-1 can prevent bone loss.(**A–I**) Representative images showing the three-dimensional trabecular structure of the contralateral distal femoral metaphysis at 4 days, 2 weeks, and 4 weeks post-fracture in mice treated with saline, MR16-1, or the control group. (**J–U**) Quantitative analysis of changes in the trabecular microarchitecture of the distal femoral metaphysis at 4 days, 2 weeks, and 4 weeks after fracture in saline treated, MR16-1 treated, and control mice (n = 5 mice/group). Error bars represent standard deviations (SDs). p-values were obtained using one-way ANOVA followed by Tukey's post hoc test.

Abbreviations: BV/TV, bone volume/tissue volume; Tb.Th, trabecular thickness; Tb.N, trabecular number; Tb.Sp, trabecular separation.

https://doi.org/10.2147/ITT.S533552

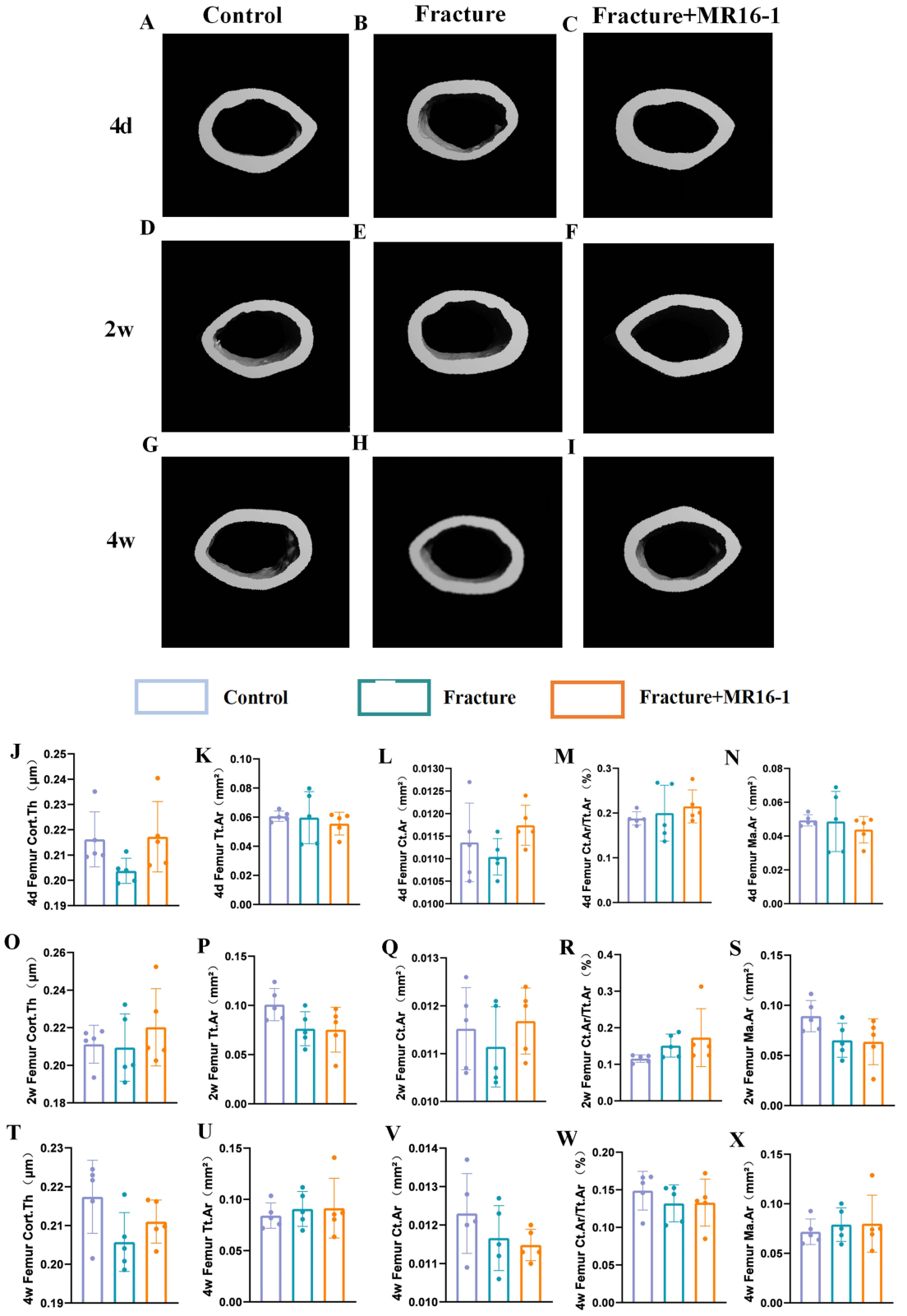

Figure 5 The cortical bone of the contralateral femoral midshaft is unaffected after femur fracture, and the use of MR16-1 does not result in further changes. (**A–I**) Representative cross-sectional images of the contralateral femoral midshaft at 4 days, 2 weeks, and 4 weeks post-fracture in mice treated with saline, MR16-1, or the control group. (**J–X**) Quantitative μCT measurements of cortical thickness (Cort.Th), total cross-sectional area (Tt.Ar), cortical area (Ct.Ar), cortical area/total cross-sectional area (Ct.Ar/Tt.Ar), and medullary area (Ma.Ar) at 4 days, 2 weeks, and 4 weeks post-fracture in mice treated with saline, MR16-1, or control (n = 5 per group). Error bars represent standard deviations (SDs). p-values were calculated using one-way ANOVA followed by Tukey's post hoc test.

Abbreviations: Ct.Ar, cortical area, Tt.Ar, total cross-sectional area, Ma.Ar, medullary area, Cort.Th, cortical thickness, and Ct.Ar/Tt.Ar, cortical area/total cross-sectional area.

https://doi.org/10.2147/ITT.S533552

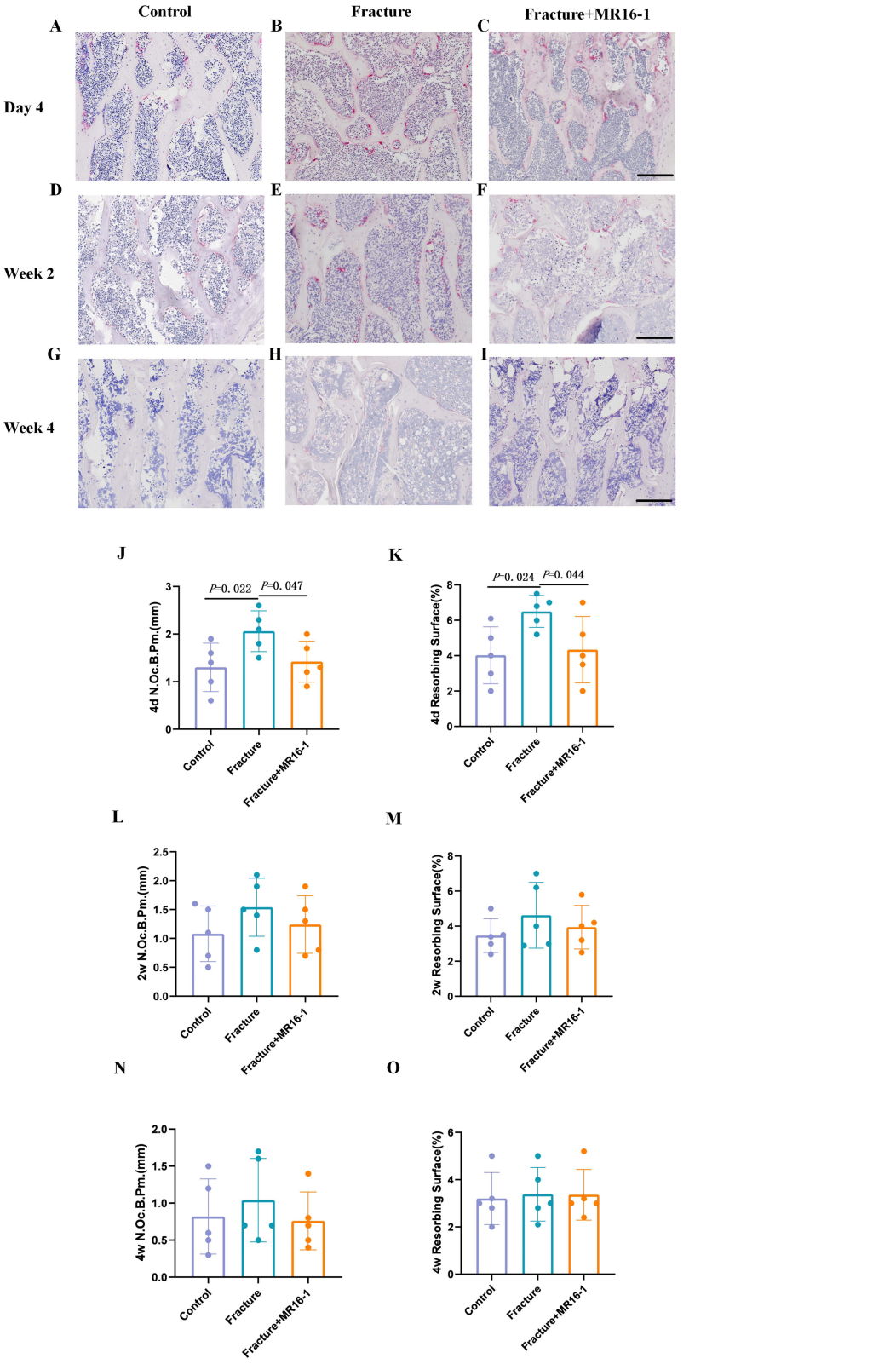

Figure 6 Osteoclast activity increases promptly after fracture, and the use of MR16-1 can counteract this effect. (**A–I**) Representative TRAP staining images of trabecular bone within the L5 vertebral body from control mice and fractured mice treated with saline or MR16-1 at (**A–C**) 4 days, (**D–F**) 2 weeks, and (**G–I**) 4 weeks post-fracture. Scale bar = 250μm. (**J** and **K**) Mice with femur fractures exhibited a significantly higher number of osteoclast and resorbed surfaces compared to control mice at 4 days post-fracture, and these effects were reversed by MR16-1 treatment (n = 5 mice/group). (**L–O**) No significant differences were found at 2 and 4 weeks after fracture (n = 5 mice/group). Error bars represent standard deviations (SDs). p-values were calculated using one-way ANOVA followed by Tukey's post hoc test.

https://doi.org/10.2147/ITT.S533552

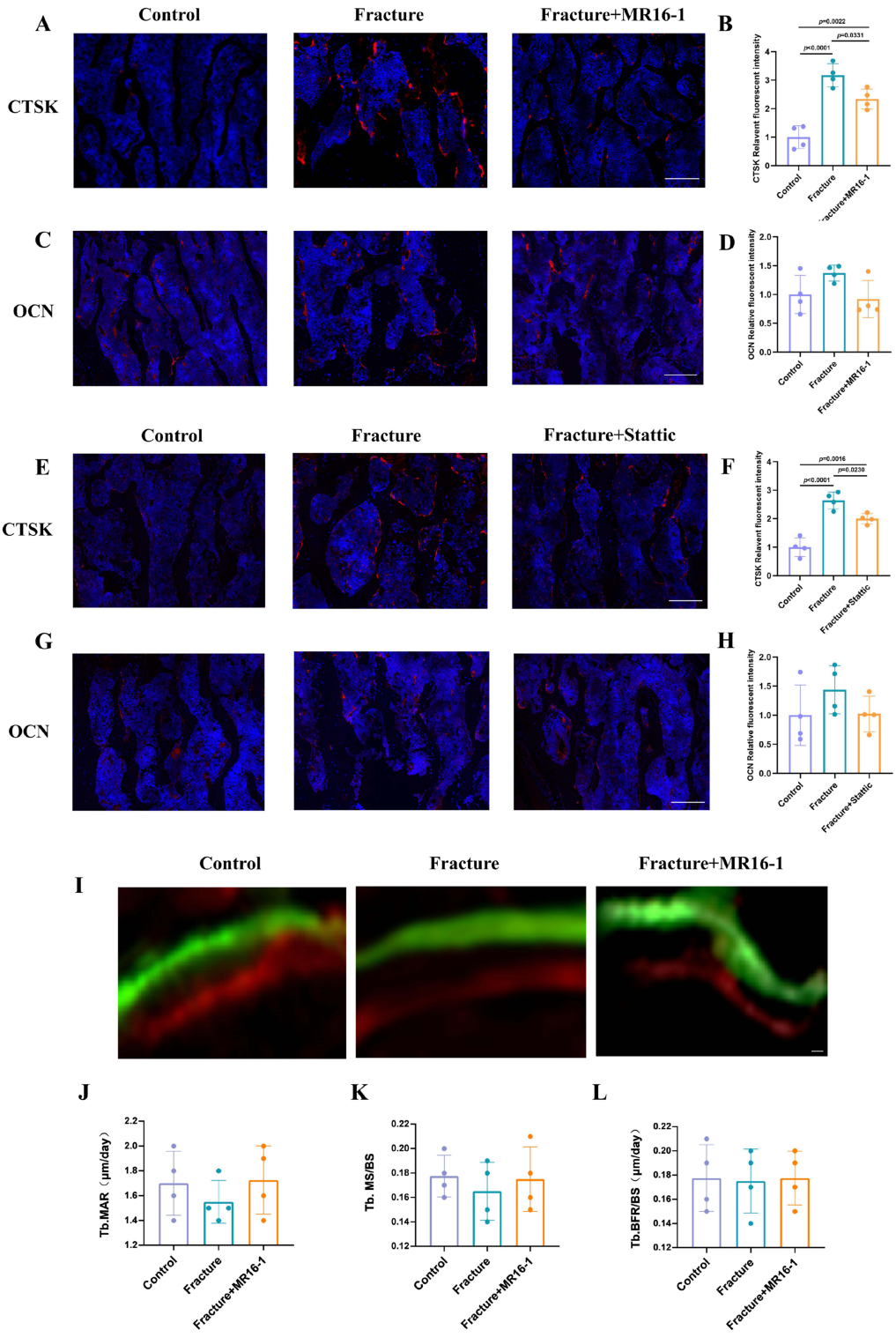

Figure 7 Osteoblast activity does not significantly change after fracture, whereas the increase in osteoclast activity can be reversed by MR16-1 or Stattic treatment.(**A**) CTSK staining in control, fracture, and MR16-1 treated mice. (**B**) Quantification of CTSK fluorescence intensity (n = 4 mice/group). (**C**) OCN staining in control, fracture, and MR16-1 treated mice. (**D**) Quantification of OCN fluorescence intensity (n = 4 mice/group). (**E**) CTSK staining in control, fracture, and Stattic treated mice. (**F**) Quantification of CTSK fluorescence intensity (n = 4 mice/group). (**G**) OCN staining in control, fracture, and Stattic treated mice. (**H**) Quantification of OCN fluorescence intensity (n = 4 mice/group). Nuclei were counterstained with DAPI (blue), and CTSK and OCN positive signals are shown in red. Scale bars: 250 μm. Error bars represent standard deviations (SDs). p-values were calculated using one-way ANOVA followed by Tukey's post hoc test. (**I**) Sequential fluorescence labeling using calcein and alizarin red in the trabecular bone of the L5 vertebral body in fractured mice, fractured mice treated with MR16-1, and control mice. Scale bar = 50 μm. (**J-L**) Dynamic histomorphometric analysis of trabecular bone formation following fracture. (n = 4 mice/group). Error bars represent standard deviations (SDs). p-values were determined using one-way ANOVA followed by Tukey's post hoc test.
Abbreviations: BFR/BS, bone formation rate per bone surface; MAR, mineral apposition rate; MS/BS, mineralizing surface per bone surface.

CTSK expression was markedly elevated in the fracture + saline group, while Stattic treatment significantly reduced its levels (Figure 7E and F). However, OCN expression remained consistent across all groups. (Figure 7G and H).

Additionally, vertebrae images labeled sequentially with calcein and alizarin red were captured 4 days post-fracture in mice treated with MR16-1 or saline. (Figure 7I). The mineral apposition rate (MAR), mineralizing surface per bone surface (MS/BS), and bone formation rate per bone surface (BFR/BS), which reflect osteoblast activity, showed no significant differences among the three groups (Figure 7J–L).

P-STAT3+ Osteocyte and RANKL Expression are Dramatically Increased After Fracture and Can Be Rescued by MR16-1

Immunohistochemical images of P-STAT3 and RANKL staining in the L5 vertebral body at 4 days post femur fracture are shown for control, fracture + saline, and fracture + MR16-1 group. The percentage of P-STAT3^{+} osteocyte markedly increased after fracture, while MR16-1 treatment significantly reduced it in the lumbar vertebrae (Figure 8A and B). Similarly, RANKL expression was significantly reduced in the fracture + MR16-1 group relative to the fracture + saline group. (Figure 8C and D).

IL-6 Stimulate Osteocyte to Secrete RANKL and Indirectly Regulates Osteocyte-Mediated Osteoclast Formation

To study the dynamic crosstalk between osteocyte and osteoclast under IL-6 stimulation, an indirect co-culture system was established. (Figure 9A). A gradual increase in RANKL expression was observed in osteocyte with increasing IL-6 concentrations (Figure 9B and C). Western blot results further revealed that osteoclast marker proteins, including CTSK and NFATC1, were significantly upregulated in the co-culture system (Figure 9D–F).

In vitro, immunofluorescence co-staining revealed that both P- STAT3 and RANKL expression in osteocyte were increased after IL-6 stimulation (Figure 9G–I). TRAP staining revealed that when osteoclast was further treated with culture medium from IL-6-treated osteocyte, the activity of osteoclast was distinctly increased with increasing concentrations of IL-6 (Figure 9J and K).

IL-6 Regulates RANKL Production by Osteocyte and Modulates Osteocyte-Mediated Osteoclast Activity Through STAT3 Phosphorylation

To investigate the role of STAT3 activation in osteocyte-mediated osteoclast formation, Stattic was used to inhibit STAT3 phosphorylation in the co-culture system (Figure 10A). IL-6 induces P-STAT3 expression in osteocyte, and this

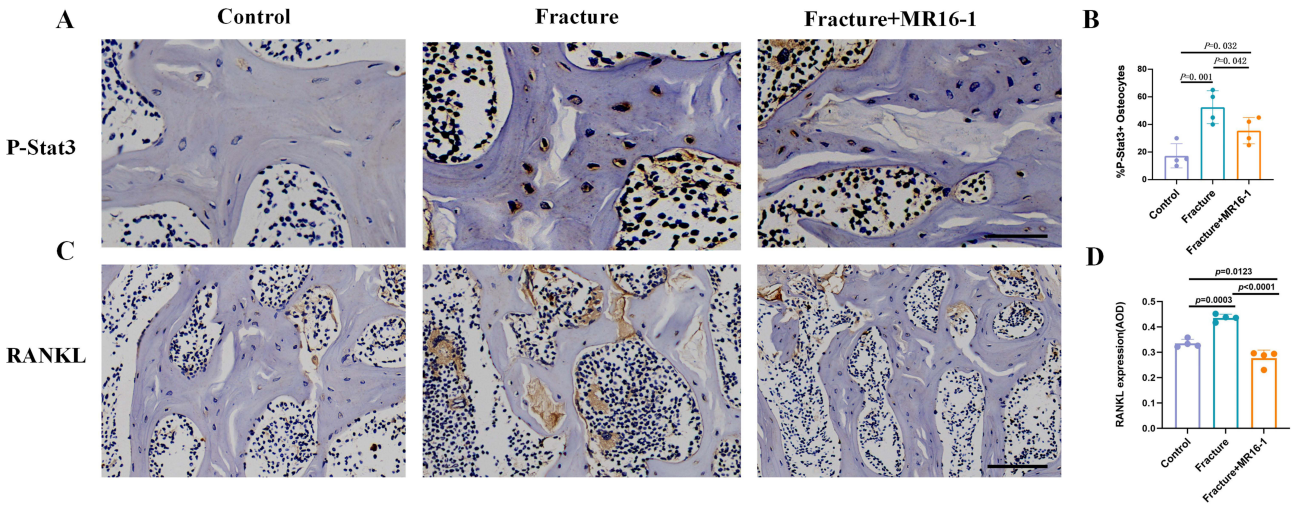

Figure 8 P-STAT3^{+} positive osteocyte and RANKL expression also increase after fracture, and these changes are attenuated by the use of MR16-1.(**A**) Representative image of osteocyte positively stained for P-STAT3 protein. Scale bar = 50 μm. (**B**) The percentage of P-STAT3^{+} osteocyte in control mice, fractured mice and fracture with MR16-1 treatment mice (n = 4 mice/group). (**C**) Immunohistochemical staining of RANKL in the cancellous bone of the L5 vertebra. Scale bar = 200 μm. (**D**) Quantification of RANKL levels of (**C**). (n = 4 mice/group) Error bars represent standard deviations (SDs). p-values were determined using one-way ANOVA followed by Tukey's post hoc test.

https://doi.org/10.2147/ITT.S533552

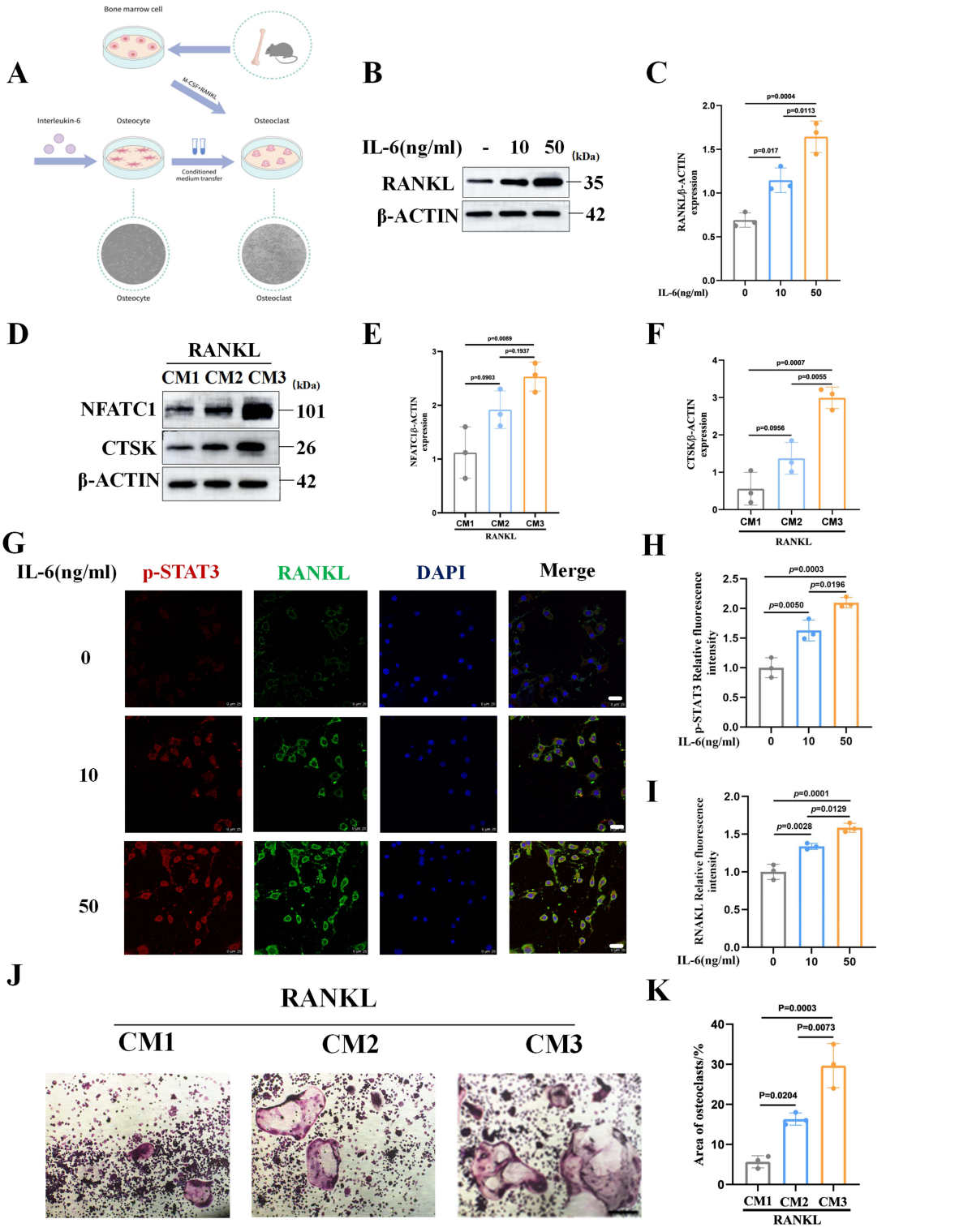

Figure 9 IL-6 can stimulate osteocyte to secrete RANKL and increase osteoclast formation in an indirect coculture system of osteocyte and osteoclast. (**A**) Schematic of the protocol for the indirect co-culture of osteocyte and osteoclast to investigate the role of IL-6. (**B**) Western blot analysis of RANKL expression in MLO-Y4 cells following IL-6 activation. (**C**) Quantification of RANKL protein levels from (**B**) (n = 3). (**D**) Western blot analysis of osteoclast-specific markers, including NFATC1 and CTSK, following indirect co-culture. (**E** and **F**) Quantification of NFATC1 and CTSK protein levels from (**D**) (n = 3). (**G**) Representative confocal microscopy images showing co-staining of p-STAT3 (red), RANKL (green), and DAPI (blue) in MLO-Y4 cells. Scale bars = 25 μm. (**H-I**) Quantitative analysis of p-STAT3 and RANKL fluorescence intensity in MLO-Y4 cells stimulated with 0, 10, or 50 ng/mL IL-6. Both p-STAT3 and RANKL levels increased in a dose-dependent manner following IL-6 treatment, with statistically significant differences observed between all groups. (n = 3). (**G**) TRAP staining to assess osteoclast differentiation. Scale bars = 200 μm. (**K**) Osteoclast area was quantified following treatment with conditioned media derived from MLO-Y4 cells stimulated with increasing concentrations (0, 10, or 50 ng/mL) of recombinant mouse IL-6, corresponding to CM1, CM2, and CM3, respectively (n = 3). Error bars represent±SDs. All data are representative of at least three independent experiments. Statistical analysis was performed using one-way ANOVA followed by Tukey's post hoc test.

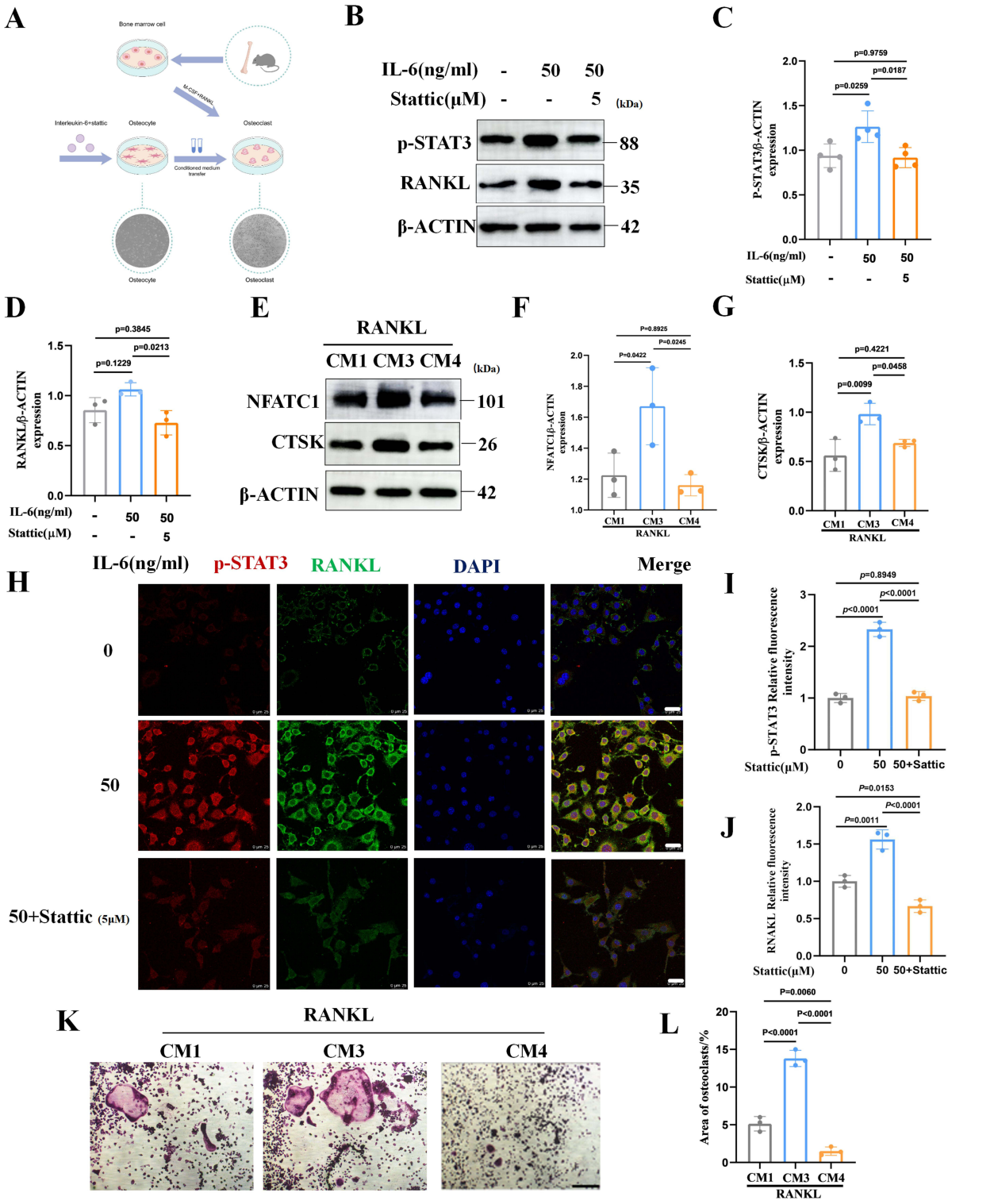

Figure 10 IL-6 stimulates osteocyte to release RANKL, which indirectly increases osteoclast activity and relies on the phosphorylation of STAT3.(**A**) Experimental setup for the indirect coculture of osteocyte and osteoclast to investigate the role of STAT3. (**B**) Western blot analysis showing the expression of RANKL and phosphorylated STAT3 (P-STAT3) in MLO-Y4 cells following IL-6 stimulation and Stattic treatment. (**C** and **D**) Quantification of P-STAT3 and RANKL protein levels from (B). (n = 3). (**E**) Western blot analysis of osteoclastic marker genes, NFATC1 and CTSK, after indirect coculture with Stattic. (**F** and **G**) Quantification of NFATC1 and CTSK protein levels from (**E**). (n = 3). (**H**) Representative confocal microscopy images displaying co-staining of P-STAT3 (red), RANKL (green), and DAPI (blue). Scale bars = 25 μm. (**I** and **J**) Quantitative fluorescence analysis of p-STAT3 and RANKL expression in MLO-Y4 cells treated with IL-6 (50 ng/mL) in the presence or absence of Stattic (5 μM). IL-6 stimulation markedly increased p-STAT3 and RANKL levels, whereas co-treatment with Stattic significantly reduced both signals (n = 3). (**K**) TRAP staining to assess osteoclast differentiation. Scale bars = 200 μm. (**K**) Quantification of osteoclast area from (**I**). (n = 3). CM1 and CM3 were conditioned media collected from MLO-Y4 cells treated with 0 and 50 ng/mL recombinant mouse IL-6, respectively. CM4 was derived from MLO-Y4 cells treated with 50 ng/mL recombinant mouse IL-6 in combination with 5 μM Stattic. Error bars represent ± SDs. Data are representative of at least three independent experiments and were analyzed using one-way ANOVA followed by Tukey's post hoc test.

https://doi.org/10.2147/ITT.S533552

expression is reduced upon treatment with Stattic, as shown by Western blotting. Likewise, STAT3 phosphorylation inhibitor diminished the capacity of IL-6 to stimulate osteocyte to secrete RANKL (Figure 10B–D). In line with this, the expression of nuclear factor of activated T cell 1 (NFATC1) and CTSK, both markers of osteoclast activity, was elevated by IL-6 stimulation but was reversed following Stattic treatment (Figure 10E–G). Co-immunofluorescence analysis demonstrated that IL-6 upregulated P- STAT3 and RANKL expression in osteocyte, while Stattic treatment effectively suppressed both proteins (Figure 10H–J). TRAP staining further demonstrated that Stattic suppressed IL-6-mediated osteocyte-driven osteoclast activity (Figure 10K and L).

IL-6/STAT3 Signaling Regulates Osteocyte-Mediated Osteoclastogenesis without Impairing Osteoblast Activity

Osteocyte were transfected with specific siSTAT3 to silence the STAT3 gene. Western blot results showed that STAT3 expression was significantly reduced in the siSTAT3 treated group compared to the control group ($p < 0.05$), indicating successful establishment of the osteocyte transfection model (Figure 11A and B). Additionally, an IL-6 stimulation experiment was performed. Quantitative analysis by Western blot revealed that, under stimulation with 50 ng/mL IL-6, the expression of phosphorylated STAT3 was markedly decreased in STAT3 silenced osteocyte compared to siSTAT3 transfected cells without IL6 treatment (Figure 11C and D). Similarly, STAT3 knockdown weakened the ability of IL-6 to promote RANKL secretion by osteocyte (Figure 11E). Furthermore, Western blot analysis revealed comparable levels of ALP, RUNX2, and OCN in MC3T3-E1 cells treated with conditioned media, with no significant differences among groups (Figure 11F–I). To further validate these findings, MC3T3-E1 cells were treated with conditioned media from IL-6 + Stattic intervention group. ALP, RUNX2, and OCN expression remained comparable across all groups, and densitometric analysis confirmed no statistically significant differences, suggesting that IL-6/STAT3 activation in osteocyte selectively promotes osteoclastogenesis without affecting osteoblast activity (Figure 11J–M).

Increased Osteoclast Activity After Fracture Can Also Be Reversed by Stattic

TRAP staining was performed on L5 vertebral trabecular bone sections from control group, fracture mice, and fracture + Stattic group, at 4 days (Supplementary Figure 1A–C), 2 weeks (Supplementary Figure 1D–F) and 4 weeks post-fracture (Supplementary Figure 1G–I). Similarly, at 4 days, we observed a significantly lower number of osteoclast and resorbed surfaces in femur fracture model mice treated with Stattic compared to those injected with saline (Supplementary Figure 1J and K). At the later time points, no notable differences were found in osteoclast count or surface resorption between the three groups (Supplementary Figure 1L–O).

Stattic Reverses Systemic Bone Loss After Fracture

Representative images of the three-dimensional trabecular bone microstructure in the L5 vertebral body were obtained at 4 days, 2 weeks, and 4 weeks under control conditions, post-femur fracture, and femur fracture with Stattic treatment, as shown in (Supplementary Figure 2A–I). Quantitative μCT analysis showed that femur fracture reduced trabecular bone volume in the L5 vertebral body at all time points (4 days, 2 weeks, and 4 weeks). Stattic treatment, however, significantly improved these bone parameters. At 4 days post-fracture, BV/TV in the L5 vertebral cancellous bone was lower in the fracture group than in control (Supplementary Figure 2J–M). Two weeks post-fracture, BV/TV and Tb.N decreased, while Tb.Sp increased markedly in the fracture group compared to control. Stattic treatment substantially improved BV/TV (Supplementary Figure 2N–Q). Four weeks after fracture, both BV/TV and Tb. Th were significantly decreased in the fracture group, but Stattic treatment alleviated this reduction, with values considerably higher than those in the fracture group (Supplementary Figure 2R–U).

Analysis of the contralateral femur diaphysis (Supplementary Figure 3A–I) showed no significant differences among the groups at 4 days post-fracture (Supplementary Figure 3J–M). However, at 2 weeks after fracture, the BV/TV, Tb. Th, and Tb. N were significantly reduced, and Tb. Sp was significantly elevated in the fracture group compared to control. Stattic treatment markedly improved BV/TV and Tb. Th (Supplementary Figure 3N–Q). At 4 weeks post-fracture, there

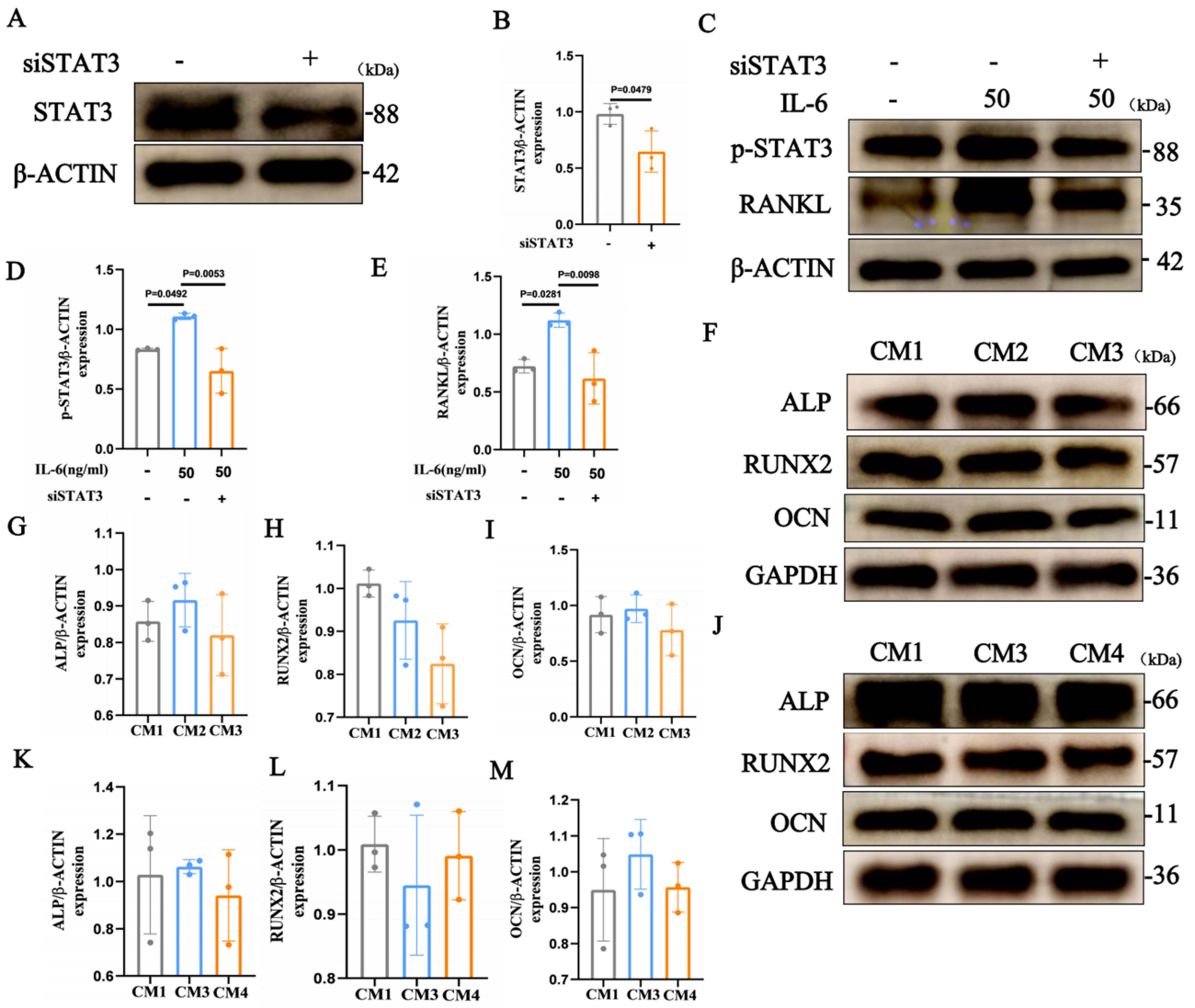

Figure 11 Osteocyte STAT3 knock-down attenuates IL-6-induced RANKL expression, whereas conditioned media from IL-6-activated osteocyte do not alter osteoblast activity. (**A**) Western blot confirming efficient STAT3 knockdown in MLO-Y4 cells. (**B**) Quantification of STAT3 protein levels (n = 3). Followed by an unpaired Student's *t*-test. (**C**) Western blot analysis of p-STAT3 and RANKL in osteocyte treated with IL-6 (50 ng/mL), with or without STAT3 siRNA. (**D** and **E**) Quantification of p-STAT3 and RANKL signals (n = 3). (**F**) Western blot analysis of ALP, RUNX2, and OCN in MC3T3-E1 cells cultured with osteocyte-conditioned media (CM1, CM2, or CM3). CM1, CM2, and CM3 were derived from MLO-Y4 cells exposed to 0, 10, or 50 ng/mL IL-6, respectively. (**G**–**I**) Quantification of ALP, RUNX2, and OCN expression in CM1-CM3 groups. (n = 3). (**J**) Western blot analysis of ALP, RUNX2, and OCN in MC3T3-E1 cells treated with CM1, CM3, or CM4. CM4 represents conditioned medium from osteocyte stimulated with 50 ng/mL recombinant mouse IL-6 and 5 μM Stattic. (**K**–**M**) Corresponding densitometric analyses for ALP, RUNX2 and OCN in the CM1, CM3 and CM4 groups (n = 3). Error bars indicate ± SD. Data are representative of at least three independent experiments and were analyzed using one-way ANOVA followed by Tukey's post hoc test.

was a dramatically decrease in Tb. N and an increase in Tb. Sp (Supplementary Figure 3R–U), but Stattic treatment mitigated these changes.

For the contralateral femur cortical shell, no significant differences were observed in cortical bone parameters, including Cort.th, Tt.Ar, Ct.Ar, Ct.Ar/Tt.Ar, and Ma. Ar, among the groups at 4 days, 2 weeks, and 4 weeks post-fracture (Supplementary Figure 4A–I, Supplementary Figure 4J–X).

Discussion

This study aimed to elucidate the immunological mechanism underlying systemic bone loss following fracture. We demonstrated that the inflammatory cytokine IL-6 plays a critical role in mediating interactions between the immune system and the skeletal system by influencing osteocyte to indirectly regulate osteoclast activity, thereby promoting bone

https://doi.org/10.2147/ITT.S533552

resorption and contributing to systemic bone loss. Specifically, IL-6 is rapidly and abundantly released following fracture as a component of the early immune response. Acting on osteocyte, IL-6 promotes STAT3 phosphorylation and induces RANKL expression, thereby amplifying osteoclast mediated bone resorption and contributing to both local and systemic bone loss. These findings highlight the role of IL-6 dependent signaling in connecting immune activation with skeletal deterioration (Figure 12).

Our findings were further validated both in vitro and in vivo through pharmacological inhibition of IL-6 signaling using MR16-1 and suppression of STAT3 phosphorylation, both of which effectively reduced osteoclast activity and bone resorption. These findings deepen our understanding of the immune mechanisms driving post-fracture bone loss and highlight a potential immunotherapeutic approach to prevent rapid systemic bone deterioration.

IL-6 is considered a common and broadly impactful inflammatory cytokine, standing out as a distinctive and prominent "star" molecule among numerous inflammatory factors. It plays vital physiological and pathological roles across nearly all major organ systems, including the nervous, skeletal, respiratory, circulatory, and digestive systems[29,35,81–86].In the skeletal system, previous studies using various inflammation associated disease models have indirectly demonstrated the harmful effects of IL-6 on bone.[37,46,51,87] Research has also revealed that IL-6 can modulate bone related cells, such as osteoblast, osteoclast, and osteocyte, to closely regulate bone metabolism.[15,44,88,89] However, the importance of IL-6 in bone loss after fracture remains unclear.

This study demonstrated that IL-6 is rapidly and robustly elevated both locally and systemically following femur fracture. Meanwhile, serum levels of TNF-α and IL-1β were also markedly elevated. Similarly, the results align with clinical observations, where a significant increase in serum IL-6, TNF-α and IL-1β levels has been reported after fracture.[90–92]

When treated with an IL-6 receptor neutralizing antibody, serum IL-6 levels were reduced at 2 and 4 weeks. However, IL-6 levels remained unchanged at 4 days. This phenomenon may be driven by two primary causes. Firstly, because anti-IL-6 receptor antibodies inhibit IL-6R-mediated clearance of IL-6 from circulation, their administration does not result in

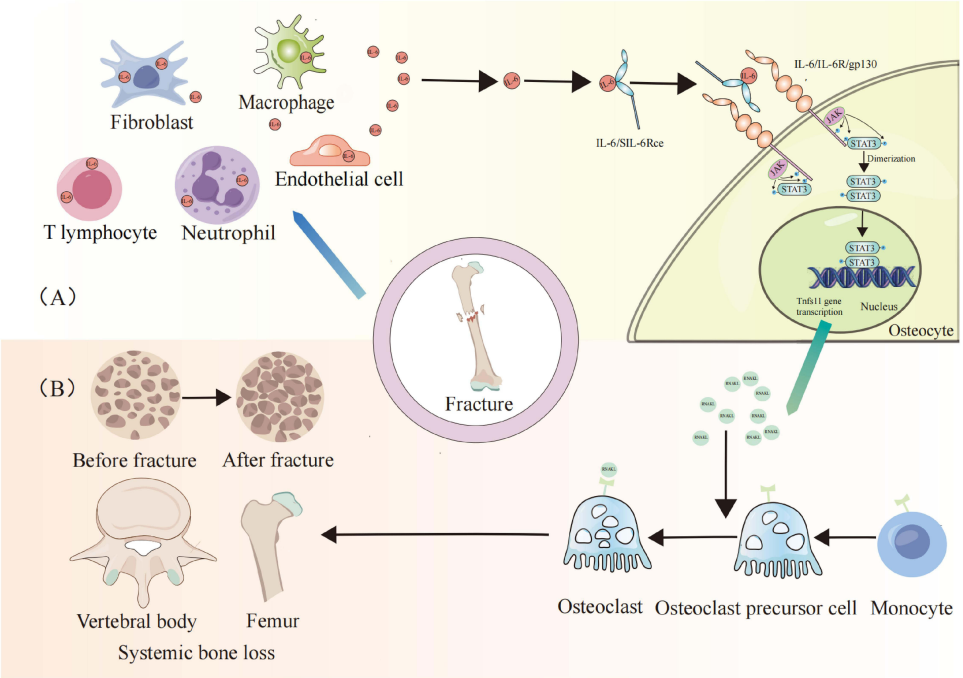

Figure 12 Summary diagram of IL-6–mediated STAT3 signaling in osteocytes promoting bone resorption following fracture. (**A**) Local fracture leads to the release of large amounts of IL-6 from various cells, including fibroblasts, macrophages, neutrophils, T lymphocytes, and endothelial cells. IL-6 binds to its receptor (IL-6R) on osteocyte, activating the STAT3 signaling pathway; (**B**) Activation of the STAT3 signaling pathway promotes RANKL expression, which in turn stimulates osteoclastogenesis, thereby contributing to systemic bone loss.

an immediate decrease in serum IL-6 levels.[93] Secondly, repeated administration may lead to drug accumulation when dosing frequency exceeds the rate of metabolism or excretion, potentially enhancing drug effect.[94]

In line with prior studies on the role of IL-6 in postmenopausal osteoporosis[33–36] and osteoarthritis related bone loss,[15,95] our results show that the use of MR16-1 could restore bone loss in the vertebral cancellous body after fracture. Interestingly, unlike IL-6, the levels of TNF-α and IL-1β did not decrease following MR16-1 treatment. The results indicate that TNF-α and IL-1β are not primary drivers of the observed phenotype, thereby underscoring the specific role of IL-6 in post-fracture bone loss. These findings suggest that, unlike other bone loss models involving multiple cytokines such as IL-6, IL-1β and TNF-α,[96–99] the acute and robust IL-6 response following fracture may have distinct effects on systemic bone loss.[100,101]

Furthermore, our study showed that femur fracture induced rapid vertebral bone loss within 4 days, as evidenced by reduced BV/TV, which was restored by MR16-1 treatment. Two weeks after femur fracture, both BV/TV and Tb.Th were reduced.

IL-6 blockade effectively prevented bone loss at this stage. At 4 weeks post-fracture, BV/TV and Tb.Th were further reduced, while Tb.Sp increased. MR16-1 treatment restored Tb.Th and reduced Tb.Sp. The results clearly demonstrate that bone loss progressively worsens over the 4 weeks period following fracture. This finding stands in contrast to previous studies that reported no significant bone loss in young mice at 4 weeks post-fracture.[7] In distal femoral cancellous bone, BV/TV and Tb.Th decreased while Tb.Sp increased at 2 weeks post-fracture. MR16-1 treatment reversed these changes. At 4 weeks, BV/TV was the only parameter that remained decreased, and the treatment effectively alleviated this reduction. Bone loss was observed in both the distal femur and vertebra, and MR16-1 treatment reduced bone loss in both regions. The specific microstructural parameters affected by bone loss and improved by treatment varied, likely due to the distinct anatomical characteristics of vertebral cancellous bone and distal femoral trabecular bone. This finding is consistent with previous research, which suggested that femur fracture can lead to compensatory bone mass increases in the contralateral femur, whereas such effects were not observed in the vertebral body.[6]

Furthermore, our findings and existing literature on post-fracture bone loss consistently indicate that bone loss predominantly occurs in trabecular bone,[73] which partially contrasts with some clinical studies reporting cortical bone loss following fractures.[102] Previous studies have indicated that the trans-signaling pathway predominantly affects trabecular bone,[87] leading us to hypothesize that IL-6 may exert its effects through this pathway. However, our experiments primarily focused on investigating bone loss by employing an IL-6 receptor blocker, which inhibits both classical and trans-signaling pathways simultaneously.[73,103] While we have partially clarified the role of IL-6 in post-fracture bone loss, further investigation into the specific signaling pathways mediating this effect would be highly valuable. In addition, the discrepancy that bone loss predominantly occurs in trabecular bone may also attributed to the factors such as differences in bone turnover rates between mice and humans, and variations in anatomical and methodological approaches and so on.[104,105]

Many studies have investigated the effects of IL-6 on bone metabolism, revealing its influence on osteoblast, osteocyte, and osteoclast.[34,43–47] Our research further revealed that the cause of bone loss after fracture may be related to the activation of osteoclast activity at 4 days after fracture, which is consistent with the findings of previous studies.[6] At this time, immunohistochemistry showed that fracture increased the number of P-STAT3^{+} osteocyte and upregulated RANKL expression, which is similar to the clinical observations that elevated serum RANKL levels were reported following fracture.[106,107] These effects were reduced after blocking IL-6. Additionally, the use of MR16-1 reduced bone resorption to efficiently restore bone loss. However, osteoclast activation was rapid but transient, with no significant changes in bone resorption observed at 2 and 4 weeks post-fracture.

Osteocyte act as a command center to regulate both bone formation and resorption, with numerous studies highlighting their upstream regulatory role and pivotal function as the primary source of RANKL, which mediates osteoclastic activity most effectively.[58,59] Similarly, our findings indicate that IL-6 stimulation leads to increased RANKL production by osteocyte. When the medium from osteocyte continues to interact with osteoclast, osteoclast activity was increased in a gradual manner, which indicates that IL-6 can establish a connection between osteocyte and osteoclast, ultimately leading to bone loss. We also found that, in vitro, osteogenic markers such as Runx2, ALP, and OCN were not significantly affected by IL-6 or the STAT3 phosphorylation inhibitor in the co-culture system. Consistently, immunofluorescence staining and dynamic histomorphometry revealed no significant changes in OCN expression or osteogenic parameters (MAR, MS/BS) after MR16-1 or Stattic treatment. These findings suggest that osteoblast are not directly involved in IL-6 mediated rapid bone loss after fracture, and

IL-6 may indirectly promote osteoclast activity via osteocyte, consistent with previous studies showing that IL-6 acts through osteocyte rather than directly targeting osteoclast or osteoblast.[64,65,108]

In previous studies, IL-6 is widely accepted and confirmed to indirectly increase the expression of osteoclastic activity by acting on osteoblast.[65,109] Furthermore, IL-6 is believed to exert its effects by activating STAT3 phosphorylation through the CRP300 receptor on the osteoblast surface, thereby increasing RANKL expression.[56,57] The IL-6/STAT3 pathway is a key regulator of diverse physiological and pathological functions in multiple organs,[110–113] with p-STAT3 activation exerting notable influence on bone metabolism.[38,68,114–116] To determine whether STAT3 phosphorylation is a critical step in IL-6-induced bone loss, we treated osteocyte with a STAT3 phosphorylation inhibitor to block phosphorylation. Our research revealed that IL-6 exerts its osteoclastic effects through osteocyte, specifically by increasing STAT3 phosphorylation and further increasing the expression of RANKL. When Stattic was used, the promotion of osteocyte RANKL expression by IL-6 and the activation of osteoclast in cocultures were significantly weakened. These findings further underscore the critical role of osteocyte in systemic bone loss after fracture. Additionally, intriguing findings from in vitro experiments indicate that IL-6 can increase RANKL expression without the addition of soluble antibodies, contradicting previous research suggesting that increased osteoclast expression requires soluble antibodies.[64]

In vitro, osteocyte was treated with Stattic, a selective STAT3 inhibitor. Western blot analysis demonstrated that this pharmacological blockade markedly suppressed the expression of osteoclast markers CTSK and NFATC1, and significantly inhibited osteoclast formation, as evidenced by TRAP staining. To further validate these findings, STAT3 was specifically knocked down in osteocyte. Western blot analysis confirmed efficient knockdown, and subsequent IL-6 stimulation resulted in a decrease in STAT3 phosphorylation. Consistently, RANKL expression was also reduced following STAT3 silencing under IL-6 stimulation.

After blocking, all the increases in bone resorption caused by IL-6 were completely attenuated. Therefore, STAT3 is considered to play a critical role in IL-6-induced bone loss. To further support our hypothesis and validate the role of STAT3, in vivo experiments were performed, which revealed that STAT3 phosphorylation blockade prevented IL-6-induced systemic bone loss after fracture. STAT3 phosphorylation inhibition also blocked IL-6-induced bone resorption. Similar to the outcome using MR16-1, bone formation markers exhibited minimal changes. Furthermore, reduced numbers of STAT3-positive and RANKL-positive osteocyte in the vertebral cancellous bone suggest that STAT3 is a downstream molecule of IL-6-induced bone loss, which is consistent with previous research indicating that STAT3 deficiency or loss can lead to consistent recovery of bone mass.[38,68,114–116]

However, given the broad inhibitory effects of Stattic on STAT3 signaling across various cell types,[34,117] which may result in unanticipated target-off effects, we intend to employ gene knockout mouse models in future experiments to delineate the mechanism with greater specificity.

Collectively, these in vivo and in vitro results highlight the crucial role of the IL-6/STAT3 phosphorylation pathway in the bone-regulatory function of osteocyte.

The harmful effects of systemic bone loss after fracture are significant. Currently, few drugs are available to treat fracture induced bone loss which was completely different from osteoporotic fractures, and the effectiveness of using anti-osteoporotic drugs for bone loss after fracture still needs further investigation.[118] Interestingly, we found that blocking IL-6 can inhibit the phosphorylation of STAT3. More importantly, this blocking can reduce osteoclast activity by inhibiting the release of RANKL from osteocyte, thereby alleviating bone loss. Furthermore, treatment with Stattic resulted in reduced bone loss. These findings imply that targeting IL-6 or STAT3 inhibition may serve as a promising strategy to prevent bone loss and lower the risk of subsequent fractures. However, previous literature has reported conflicting results regarding the impact of IL-6 blockade on fracture healing. While some studies suggest that IL-6 inhibition promotes healing,[42] others indicate it may impair the process.[119] These discrepancies may be attributed to differences in the timing of IL-6 blockade, the fracture models used, and the specific time points assessed[42,119] Therefore, further investigation into the effects of IL-6 blockade on local fracture healing holds significant clinical relevance and research value.

Our study possesses several strengths. First, considering the significantly increased risk of recurrent fractures and the pronounced bone loss following an initial fracture, we dynamically analyzed the characteristics of bone loss at multiple time points. More importantly, we are among the first to elucidate the immunological mechanisms driving systemic bone loss post-fracture. We emphasize the critical immunoregulatory role of the inflammatory cytokine IL-6 in initiating rapid systemic bone

loss. Additionally, our study highlights the pivotal function of osteocyte in post-fracture bone remodeling, clarifying how IL-6 influences osteocyte to modulate osteoclast activity. This finding advances the understanding of osteocyte-mediated immune regulation in bone metabolism. Furthermore, we established that the IL-6/STAT3 signaling axis is a key mediator of systemic bone loss. And we demonstrated that targeting this pathway with inhibitors effectively mitigates osteoclast activation and bone resorption. These insights provide potential immunotherapeutic strategies for preventing post-fracture bone loss and reducing the likelihood of recurrent fractures.

This study also has several limitations. First, while our hypotheses were examined in a murine model, species-specific differences between mice and humans may affect the translatability of the findings. Future studies should incorporate larger animal models (eg, minipigs or dogs) and human fracture samples to validate IL-6 pathway activation in clinical settings. Second, while we observed a rapid and robust increase in IL-6 following fracture, the upstream regulators of IL-6 in bone loss remain to be elucidated. Third, Stattic is a broad STAT3 inhibitor that may affect various STAT3-expressing cell types in vivo. As our current design does not fully control for this, future studies using STAT3 knockout mice are warranted to provide more precise mechanistic insights. Finally, we selected the 4-week time point for experimentation. This choice was based on the near completion of fracture healing during this period,[120,121] indicating its adequacy for mechanistic investigation. Nevertheless, extending the observation period to assess delayed effects remains valuable, and future studies will address this.

Conclusion

IL-6 drives rapid systemic bone loss after fracture by promoting STAT3 phosphorylation in osteocyte and upregulating RANKL, thereby enhancing osteoclast activity and bone resorption. These findings suggest that the IL-6/STAT3/RANKL axis may serve as a critical link between immune signaling and skeletal homeostasis, as well as a promising therapeutic target for preventing inflammation induced bone loss and fracture recurrence. Future studies should focus on translating these insights into clinical strategies for improving bone healing after fracture.

Data Sharing Statement

Data supporting the findings of this study can be obtained from the corresponding authors upon reasonable request.

Ethics Approval

All animal experiments were conducted in compliance with the ethical guidelines established by the Ethics Committee for the Care and Use of Laboratory Animals at Shandong Provincial Hospital Affiliated to Shandong First Medical University. The procedures were conducted in strict accordance with the internationally recognized Five Freedoms for the welfare of laboratory animals: freedom from hunger and thirst; freedom from discomfort; freedom from pain, injury, and disease; freedom from fear and distress; and freedom to express normal behavior.

Acknowledgments

The authors express their gratitude to AJE for their assistance in language editing of an earlier draft of this manuscript.

Author Contributions

All authors made a significant contribution to the work reported, whether that is in the conception, study design, execution, acquisition of data, analysis and interpretation, or in all these areas; took part in drafting, revising or critically reviewing the article; gave final approval of the version to be published; have agreed on the journal to which the article has been submitted; and agree to be accountable for all aspects of the work.

Funding

This study was funded by the National Natural Science Foundation of China (Project No. 82202701) and the Natural Science Foundation of Shandong Province (Grant No. ZR2022QH184).

Disclosure

The authors declare that they have no competing interests in this work.

References

1. Bogoch E, Marcano-Fernández FA, Schemitsch EH, et al. High rates of imminent subsequent fracture after femoral neck fracture in the elderly. *The Journal of Bone and Joint Surgery. American Volume*. 2022;104(22):1984–1992. doi:10.2106/jbjs.22.00088
2. Axelsson KF, Litsne H, Lorentzon M. The Importance of recent prevalent fracture site for imminent risk of fracture - a retrospective, nationwide cohort study of older swedish men and women. *J Bone Miner Res*. 2023;38(6):851–859. doi:10.1002/jbmr.4806
3. Bégin MJ, Audet MC, Chevalley T, et al. Fracture risk following an atypical femoral fracture. *J Bone Miner Res*. 2022;37(1):87–94. doi:10.1002/jbmr.4461
4. Patel R, Judge A, Johansen A, et al. Following Hip fracture, hospital organisational factors associated with prescription of anti-osteoporosis medication on discharge, to address imminent refracture risk: a record-linkage study. *J Bone Miner Res*. 2024. doi:10.1093/jbmr/zjae100
5. Praveen AD, Aspelund T, Ferguson SJ, et al. Refracture and mortality risk in the elderly with osteoporotic fractures: the AGES-Reykjavik study. *Osteoporosis Int*. 2024. doi:10.1007/s00198-024-07096-3
6. Zhang C, Zhu J, Jia J, et al. Effect of single versus multiple fractures on systemic bone loss in mice. *J Bone Miner Res*. 2021;36(3):567–578. doi:10.1002/jbmr.4211
7. Emami AJ, Toupadakis CA, Telek SM, Fyhrie DP, Yellowley CE, Christiansen BA. Age dependence of systemic bone loss and recovery following femur fracture in mice. *J Bone Miner Res*. 2019;34(1):157–170. doi:10.1002/jbmr.3579
8. Osipov B, Paralkar MP, Emami AJ, et al. Sex differences in systemic bone and muscle loss following femur fracture in mice. *J Orthop Res*. 2022;40(4):878–890. doi:10.1002/jor.25116
9. Ely EV, Osipov B, Emami AJ, Christiansen BA. Region-dependent bone loss in the lumbar spine following femoral fracture in mice. *Bone*. 2020;140:115555. doi:10.1016/j.bone.2020.115555
10. Wu D, Cline-Smith A, Shashkova E, Perla A, Katyal A, Aurora R. T-cell mediated inflammation in postmenopausal osteoporosis. *Front Immunol*. 2021;12:687551. doi:10.3389/fimmu.2021.687551
11. Guo M, Liu H, Yu Y, et al. Lactobacillus rhamnosus GG ameliorates osteoporosis in ovariectomized rats by regulating the Th17/Treg balance and gut microbiota structure. *Gut Microbes*. 2023;15(1):2190304. doi:10.1080/19490976.2023.2190304
12. Zhang J, Jiang J, Qin Y, Zhang Y, Wu Y, Xu H. Systemic immune-inflammation index is associated with decreased bone mass density and osteoporosis in postmenopausal women but not in premenopausal women. *Endocr Connect*. 12(2). doi:10.1530/ec-22-0461
13. Riegger J, Schoppa A, Ruths L, Haffner-Luntzer M, Ignatius A. Oxidative stress as a key modulator of cell fate decision in osteoarthritis and osteoporosis: a narrative review. *Cell Mol Biol Lett*. 28(1):76. doi:10.1186/s11658-023-00489-y
14. Doi K, Murata K, Ito S, et al. Role of lysine-specific demethylase 1 in metabolically integrating osteoclast differentiation and inflammatory bone resorption through hypoxia-inducible factor 1α and E2F1. *Arthritis Rheumatol*. 2022;74(6):948–960. doi:10.1002/art.42074
15. Yokota K, Sato K, Miyazaki T, et al. Characterization and function of tumor necrosis factor and interleukin-6-induced osteoclasts in rheumatoid arthritis. *Arthritis Rheumatol*. 2021;73(7):1145–1154. doi:10.1002/art.41666
16. Einhorn TA, Gerstenfeld LC. Fracture healing: mechanisms and interventions. *Nat Rev Rheumatol*. 2015;11(1):45–54. doi:10.1038/nrrheum.2014.164
17. Goodman SB, Maruyama M. Inflammation, bone healing and osteonecrosis: from bedside to bench. *J Inflamm Res*. 2020;13:913–923. doi:10.2147/jir.S281941
18. Zheng J, Yao Z, Xue L, Wang D, Tan Z. The role of immune cells in modulating chronic inflammation and osteonecrosis. *Front Immunol*. 2022;13:1064245. doi:10.3389/fimmu.2022.1064245
19. Fang B, Wang D, Zheng J, et al. Involvement of tumor necrosis factor alpha in steroid-associated osteonecrosis of the femoral head: friend or foe? *Stem Cell Res Ther*. 10(1):5. doi:10.1186/s13287-018-1112-x
20. Baral B, Parajuli M, Pinilla J, Quintanilha B, Baral B, Molina FC. Efficacy and safety of tocilizumab in polymyalgia rheumatica: a systematic review and meta-analysis of randomized controlled trials. *ARP Rheumatol*. 2025;4(2):145–153.
21. Onishi A, Tanaka M, Fujii T, et al. Comparative effectiveness of subcutaneous sarilumab 200 mg biweekly, subcutaneous Tocilizumab 162 mg biweekly, and intravenous Tocilizumab 8 mg/kg every 4 weeks in patients with rheumatoid arthritis: a prospective cohort study. *Arthritis Res Ther*. 27(1):52. doi:10.1186/s13075-025-03514-x
22. Parisi S, Ditto MC, Ghellere F, et al. Update on tocilizumab in rheumatoid arthritis: a narrative review. *Front Immunol*. 2025;16:1470488. doi:10.3389/fimmu.2025.1470488
23. Xie M, Liu Q, Yuan H, et al. Case Report: intra-articular injection of tocilizumab for arthritis treatment in chronic graft-vs.-host disease. *Front Pediatr*. 2025;13:1515706. doi:10.3389/fped.2025.1515706
24. Herrera-Ruiz A, Tovar BB, García RG, Tamez MFL, Mamidi N. Nanomaterials-incorporated chemically modified gelatin methacryloyl-based biomedical composites: a novel approach for bone tissue engineering. *Pharmaceutics*. 14(12). doi:10.3390/pharmaceutics14122645
25. Mamidi N, González-Ortiz A, Romo IL, Barrera EV. Development of functionalized carbon nano-onions reinforced zein protein hydrogel interfaces for controlled drug release. *Pharmaceutics*. 11(12). doi:10.3390/pharmaceutics11120621
26. Mamidi N, Ijadi F, Norahan MH. Leveraging the recent advancements in GelMA scaffolds for bone tissue engineering: an assessment of challenges and opportunities. *Biomacromolecules*. 2024;25(4):2075–2113. doi:10.1021/acs.biomac.3c00279
27. Alogna A, Koepp KE, Sabbah M, et al. Interleukin-6 in patients with heart failure and preserved ejection fraction. *JACC Heart Fail*. 2023;11(11):1549–1561. DOI:10.1016/j.jchf.2023.06.031
28. Alter C, Henseler AS, Owenier C, et al. IL-6 in the infarcted heart is preferentially formed by fibroblasts and modulated by purinergic signaling. *J Clin Invest*. 2023;133(11). doi:10.1172/jci163799
29. Qing H, Desrouleaux R, Israni-Winger K, et al. Origin and function of stress-induced Il-6 in murine models. *Cell*. 182(2):372–387.e14. doi:10.1016/j.cell.2020.05.054
30. Rose-John S, Jenkins BJ, Garbers C, Moll JM, Scheller J. Targeting IL-6 trans-signalling: past, present and future prospects. *Nat Rev Immunol*. 2023;23(10):666–681. doi:10.1038/s41577-023-00856-y
31. Zhang S, Takaku M, Zou L, et al. Reversing SKI-SMAD4-mediated suppression is essential for T(H)17 cell differentiation. *Nature*. 551(7678):105–109. doi:10.1038/nature24283

32. Chen W, Cui W, Wu J, et al. Blocking IL-6 signaling improves glucose tolerance via SLC39A5-mediated suppression of glucagon secretion. *Metabolism*. 2023;146:155641. doi:10.1016/j.metabol.2023.155641
33. Fischer V, Haffner-Luntzer M. Interaction between bone and immune cells: implications for postmenopausal osteoporosis. *Semin Cell Dev Biol*. 2022;123:14–21. doi:10.1016/j.semcdb.2021.05.014
34. Wang T, He C. TNF-α and IL-6: the link between immune and bone system. *Curr Drug Targets*. 2020;21(3):213–227. doi:10.2174/1389450120666190821161259
35. Takeuchi T, Yoshida H, Tanaka S. Role of interleukin-6 in bone destruction and bone repair in rheumatoid arthritis. *Autoimmunity Rev*. 2021;20(9):102884. doi:10.1016/j.autrev.2021.102884
36. Shi X, Jiang J, Hong R, Xu F, Dai S. Circulating IGFBP-3 and Interleukin 6 as predictors of osteoporosis in postmenopausal women: a cross-sectional study. *Mediators Inflammation*. 2023;2023:2613766. doi:10.1155/2023/2613766
37. Ren Y, Deng Z, Gokani V, et al. Anti-Interleukin-6 therapy decreases hip synovitis and bone resorption and increases bone formation following ischemic osteonecrosis of the femoral head. *J Bone Miner Res*. 2021;36(2):357–368. doi:10.1002/jbmr.4191
38. Isojima T, Walker EC, Poulton IJ, et al. G-CSF receptor deletion amplifies cortical bone dysfunction in mice with STAT3 hyperactivation in osteocytes. *J Bone Miner Res*. 2022;37(10):1876–1890. doi:10.1002/jbmr.4654
39. He B, Yin X, Hao D, et al. Blockade of IL-6 alleviates bone loss induced by modeled microgravity in mice. *Can J Physiol Pharmacol*. 2020;98(10):678–683. doi:10.1139/cjpp-2019-0632
40. Roberts JL, Chiedo B, Drissi H. Systemic inflammatory and gut microbiota responses to fracture in young and middle-aged mice. *Geroscience*. 2023;45(6):3115–3129. doi:10.1007/s11357-023-00963-7
41. Molitoris KH, Balu AR, Huang M, Baht GS. The impact of age and sex on the inflammatory response during bone fracture healing. *JBMR Plus*. 2024;8(5):ziae023. doi:10.1093/jbmrpl/ziae023
42. Coates BA, McKenzie JA, Yoneda S, Silva MJ. Interleukin-6 (IL-6) deficiency enhances intramembranous osteogenesis following stress fracture in mice. *Bone*. 2021;143:115737. doi:10.1016/j.bone.2020.115737
43. Deng Z, Zhang R, Li M, et al. STAT3/IL-6 dependent induction of inflammatory response in osteoblast and osteoclast formation in nanoscale wear particle-induced aseptic prosthesis loosening. *Biomater Sci*. 9(4):1291–1300. doi:10.1039/d0bm01256d
44. Tirado-Cabrera I, Martin-Guerrero E, Heredero-Jimenez S, Ardura JA, Gortázar AR. PTH1R translocation to primary cilia in mechanically-stimulated ostecytes prevents osteoclast formation via regulation of CXCL5 and IL-6 secretion. *J Cell Physiol*. 2022;237(10):3927–3943. doi:10.1002/jcp.30849
45. Chang PY, Wu HK, Chen YH, et al. Interleukin-6 transiently promotes proliferation of osteoclast precursors and stimulates the production of inflammatory mediators. *Mol Biol Rep*. 2022;49(5):3927–3937. doi:10.1007/s11033-022-07243-1
46. NA S. Influences of the IL-6 cytokine family on bone structure and function. *Cytokine*. 2021;146:155655. doi:10.1016/j.cyto.2021.155655
47. Palmisano B, Riminucci M, Karsenty G. Interleukin-6 signaling in osteoblasts regulates bone remodeling during exercise. *Bone*. 2023;176:116870. doi:10.1016/j.bone.2023.116870
48. Kurozumi A, Nakano K, Yamagata K, Okada Y, Nakayamada S, Tanaka Y. IL-6 and sIL-6R induces STAT3-dependent differentiation of human VSMCs into osteoblast-like cells through JMJD2B-mediated histone demethylation of RUNX2. *Bone*. 2019;124:53–61. doi:10.1016/j.bone.2019.04.006
49. Karadag A, AM S, Croucher PI. Human myeloma cells promote the recruitment of osteoblast precursors: mediation by interleukin-6 and soluble interleukin-6 receptor. *J Bone Miner Res*. 2000;15(10):1935–1943. doi:10.1359/jbmr.2000.15.10.1935
50. Kaneshiro S, Ebina K, Shi K, et al. IL-6 negatively regulates osteoblast differentiation through the SHP2/MEK2 and SHP2/Akt2 pathways in vitro. *J Bone Miner Metab*. 2014;32(4):378–392. doi:10.1007/s00774-013-0514-1
51. Peruzzi B, Cappariello A, Del FA, Rucci N, De Benedetti F, Teti A. c-Src and IL-6 inhibit osteoblast differentiation and integrate IGFBP5 signalling. *Nat Commun*. 3:630. doi:10.1038/ncomms1651
52. Franchimont N, Wertz S, Malaise M. Interleukin-6: an osteotropic factor influencing bone formation? *Bone*. 2005;37(5):601–606. doi:10.1016/j.bone.2005.06.002
53. Nishimura R, Moriyama K, Yasukawa K, GR M, Yoneda T. Combination of interleukin-6 and soluble interleukin-6 receptors induces differentiation and activation of JAK-STAT and MAP kinase pathways in MG-63 human osteoblastic cells. *J Bone Miner Res*. 1998;13(5):777–785. doi:10.1359/jbmr.1998.13.5.777
54. Sellin ML, Klinder A, Bergschmidt P, Bader R, Jonitz-Heincke A. IL-6-induced response of human osteoblasts from patients with rheumatoid arthritis after inhibition of the signaling pathway. *Clin Exp Med*. 2023;23(7):3479–3499. doi:10.1007/s10238-023-01103-3
55. Bakker AD, Kulkarni RN, Klein-Nulend J, Lems WF. IL-6 alters osteocyte signaling toward osteoblasts but not osteoclasts. *J Dent Res*. 2014;93(4):394–399. doi:10.1177/0022034514522485
56. Udagawa N, Takahashi N, Katagiri T, et al. Interleukin (IL)-6 induction of osteoclast differentiation depends on IL-6 receptors expressed on osteoblastic cells but not on osteoclast progenitors. *J Exp Med*. 182(5):1461–1468. doi:10.1084/jem.182.5.1461
57. Liu XH, Kirschenbaum A, Yao S, Levine AC. Interactive effect of interleukin-6 and prostaglandin E2 on osteoclastogenesis via the OPG/RANKL/RANK system. *Ann N Y Acad Sci*. 2006;1068:225–233. doi:10.1196/annals.1346.047
58. Delgado-Calle J, Bellido T. The osteocyte as a signaling cell. *Physiol Rev*. 2022;102(1):379–410. doi:10.1152/physrev.00043.2020
59. Robling AG, Bonewald LF. The Osteocyte: new Insights. *Annu Rev Physiol*. 82:485–506. doi:10.1146/annurev-physiol-021119-034332
60. Kittaka M, Yoshimoto T, Levitan ME, et al. Osteocyte RANKL drives bone resorption in mouse ligature-induced periodontitis. *J Bone Miner Res*. 2023;38(10):1521–1540. doi:10.1002/jbmr.4897
61. Andreev D, Liu M, Weidner D, et al. Osteocyte necrosis triggers osteoclast-mediated bone loss through macrophage-inducible C-type lectin. *J Clin Invest*. 130(9):4811–4830. doi:10.1172/jci134214
62. Plotkin LI, Bellido T. Osteocytic signalling pathways as therapeutic targets for bone fragility. *Nat Rev Endocrinol*. 2016;12(10):593–605. doi:10.1038/nrendo.2016.71
63. Shi T, Shen S, Shi Y, et al. Osteocyte-derived sclerostin impairs cognitive function during ageing and Alzheimer's disease progression. *Nat Metab*. 2024;6(3):531–549. doi:10.1038/s42255-024-00989-x
64. Wu Q, Zhou X, Huang D, Ji Y, Kang F. IL-6 enhances osteocyte-mediated osteoclastogenesis by promoting JAK2 and RANKL activity in vitro. *Cellular Physiol Biochem*. 2017;41(4):1360–1369. doi:10.1159/000465455

65. McGregor NE, Murat M, Elango J, et al. IL-6 exhibits both cis- and trans-signaling in osteocytes and osteoblasts, but only trans-signaling promotes bone formation and osteoclastogenesis. *J Biol Chem*. 294(19):7850–7863. doi:10.1074/jbc.RA119.008074
66. Zhu L, Wang Z, Sun X, et al. STAT3/mitophagy axis coordinates macrophage NLRP3 inflammasome activation and inflammatory bone loss. *J Bone Miner Res*. 2023;38(2):335–353. doi:10.1002/jbmr.4756
67. Yang Y, Chung MR, Zhou S, et al. STAT3 controls osteoclast differentiation and bone homeostasis by regulating NFATc1 transcription. *J Biol Chem*. 294(42):15395–15407. doi:10.1074/jbc.RA119.010139
68. Gong X, Sun S, Yang Y, et al. Osteoblastic STAT3 is crucial for orthodontic force driving alveolar bone remodeling and tooth movement. *J Bone Miner Res*. 2023;38(1):214–227. doi:10.1002/jbmr.4744
69. Gu JH, Chae MY, Choi JJ, Duc TC, Son CG, Lee EJ. Deer antler velvet (Cervus elaphus sibiricus) promotes fracture healing via partial BMP2-Smad mediated osteoblast differentiation. *J Orthopaedic Surg Res*. 20(1):70. doi:10.1186/s13018-024-05426-z
70. Kobbe P, Vodovotz Y, Kaczorowski DJ, Mollen KP, Billiar TR, Pape HC. Patterns of cytokine release and evolution of remote organ dysfunction after bilateral femur fracture. *Shock*. 2008;30(1):43–47. doi:10.1097/SHK.0b013e31815d190b
71. Choi RY, Kim IW, Ji M, et al. Protaetia brevitarsis seulensis larvae ethanol extract inhibits RANKL-stimulated osteoclastogenesis and ameliorates bone loss in ovariectomized mice. *Biomed Pharmacothe*. 2023;165:115112. doi:10.1016/j.biopha.2023.115112
72. Zhu J, Liu C, Jia J, et al. Short-term caloric restriction induced bone loss in both axial and appendicular bones by increasing adiponectin. *Ann N Y Acad Sci*. 2020;1474(1):47–60. doi:10.1111/nyas.14380
73. Kuroyanagi G, Kamiya N, Yamaguchi R, Kim HKW. Interleukin-6 receptor blockade improves bone healing following ischemic osteonecrosis in adolescent mice. *Osteoarthritis Cartilage Open*. 2023;5(4):100386. doi:10.1016/j.ocarto.2023.100386
74. Yokota T, Omachi K, Suico MA, et al. STAT3 inhibition attenuates the progressive phenotypes of Alport syndrome mouse model. *Nephrol Dial Transplant*. 33(2):214–223. doi:10.1093/ndt/gfx246
75. Cao Y, Lin X, Gao D, Yang J, Miao H, Li T. Inhibition of STAT3 phosphorylation attenuates perioperative neurocognitive disorders in mice with D-galactose-induced aging by regulating pro-inflammatory reactive astrocytes. *Int Immunopharmacol*. 148:114095. doi:10.1016/j.intimp.2025.114095
76. Millot P, San C, Bennana E, et al. STAT3 inhibition protects against neuroinflammation and BACE1 upregulation induced by systemic inflammation. *Immunol Lett*. 2020;228:129–134. doi:10.1016/j.imlet.2020.10.004
77. Dong R, Wei J, Tian S, et al. Single-cell RNA transcriptomics reveals Du-Zhong-Wan promotes osteoporotic fracture healing via YAP/β-catenin /VEGF axis in BMSCs. *Phytomedicine*. 2024;135:155572. doi:10.1016/j.phymed.2024.155572
78. Jähn K, Lara-Castillo N, Brotto L, et al. Skeletal muscle secreted factors prevent glucocorticoid-induced osteocyte apoptosis through activation of β-catenin. *European cells & materials*. 24. 197–209. doi:10.22203/ecm.v024a14
79. Song X, Tang Y, Zhu J, et al. HIF-1α induces hypoxic apoptosis of MLO-Y4 osteocytes via JNK/caspase-3 pathway and the apoptotic-osteocyte -mediated osteoclastogenesis in vitro. *Tissue Cell*. 2020;67:101402. doi:10.1016/j.tice.2020.101402
80. Chen X, Dou J, Fu Z, et al. Macrophage M1 polarization mediated via the IL-6/STAT3 pathway contributes to apical periodontitis induced by Porphyromonas gingivalis. *J Appl Oral Sci*. 2022;30:e20220316. doi:10.1590/1678-7757-2022-0316
81. TM K, BK P, DE L. Interleukin 6 as an energy allocator in muscle tissue. *Nat Metab*. 2022;4(2):170–179. doi:10.1038/s42255-022-00538-4
82. Cho DC, Brennan HJ, Johnson RW, et al. Bone corticalization requires local SOCS3 activity and is promoted by androgen action via interleukin-6. *Nat Commun*. 2017;8(1):806. doi:10.1038/s41467-017-00920-x
83. Odell ID, Agrawal K, Sefik E, et al. IL-6 trans-signaling in a humanized mouse model of scleroderma. *Proc Natl Acad Sci USA*. 120(37): e2306965120. doi:10.1073/pnas.2306965120
84. McElvaney OJ, Curley GF, Rose-John S, McElvaney NG. Interleukin-6: obstacles to targeting a complex cytokine in critical illness. *Lancet Respir Med*. 2021;9(6):643–654. doi:10.1016/s2213-2600(21)00103-x
85. Choi BR, Johnson KR, Maric D, DB M. Monocyte-derived IL-6 programs microglia to rebuild damaged brain vasculature. *Nat Immunol*. 2023;24(7):1110–1123. doi:10.1038/s41590-023-01521-1
86. Tyrrell DJ, Goldstein DR. Ageing and atherosclerosis: vascular intrinsic and extrinsic factors and potential role of IL-6. *Nat Rev Cardiol*. 2021;18(1):58–68. doi:10.1038/s41569-020-0431-7
87. Lazzaro L, Tonkin BA, Poulton IJ, McGregor NE, Ferlin W, Sims NA. IL-6 trans-signalling mediates trabecular, but not cortical, bone loss after ovariectomy. *Bone*. 2018;112:120–127. doi:10.1016/j.bone.2018.04.015
88. Cheung WY, Simmons CA, You L. Osteocyte apoptosis regulates osteoclast precursor adhesion via osteocytic IL-6 secretion and endothelial ICAM-1 expression. *Bone*. 2012;50(1):104–110. doi:10.1016/j.bone.2011.09.052
89. Kurokouchi K, Kambe F, Yasukawa K, et al. TNF-alpha increases expression of IL-6 and ICAM-1 genes through activation of NF-kappaB in osteoblast-like ROS17/2.8 cells. *J Bone Miner Res*. 1998;13(8):1290–1299. doi:10.1359/jbmr.1998.13.8.1290
90. Câmara SMA, Hochberg MC, Miller R, et al. Sustained IL-6 and sTNF-αR1 levels after Hip fracture predict 5-year mortality: a prospective cohort study from the baltimore hip studies. *J Am Geriatr Soc*. 2024;72(9):2644–2655. doi:10.1111/jgs.19018
91. Robitaille B, Herrero BA, Jodoin M, Briand MM, Rouleau DM, De BL. A pilot investigation on inflammatory markers and theta burst stimulation protocol interaction along a three-month recovery course following an isolated upper limb fracture. *Cytokine*. 188:156885. doi:10.1016/j.cyto.2025.156885
92. Ye C, Shen J, Zhang C, Hu C. Impact of intraoperative dexmedetomidine on postoperative delirium and pro-inflammatory cytokine levels in elderly patients undergoing thoracolumbar compression fracture surgery: a prospective, randomized, placebo-controlled clinical trial. *Medicine*. 103(18):e37931. doi:10.1097/md.0000000000037931
93. Uchiyama Y, Yoshida H, Koike N, et al. Anti-IL-6 receptor antibody increases blood IL-6 level via the blockade of IL-6 clearance, but not via the induction of IL-6 production. *Int Immunopharmacol*. 2008;8(11):1595–1601. doi:10.1016/j.intimp.2008.07.002
94. Brocks DR, Mehvar R. Rate and extent of drug accumulation after multiple dosing revisited. *Clin Pharmacokinet*. 2010;49(7):421–438. doi:10.2165/11531190-000000000-00000
95. Symons RA, Colella F, Collins FL, et al. Targeting the IL-6-Yap-Snail signalling axis in synovial fibroblasts ameliorates inflammatory arthritis. *Ann Rheumatic Dis*. 2022;81(2):214–224. doi:10.1136/annrheumdis-2021-220875
96. Chen MH, Wang YH, Sun BJ, et al. HIF-1α activator DMOG inhibits alveolar bone resorption in murine periodontitis by regulating macrophage polarization. *Int Immunopharmacol*. 2021;99:107901. doi:10.1016/j.intimp.2021.107901

97. Tang L, Gao X, Yang X, et al. Ladder-climbing training prevents bone loss and microarchitecture deterioration in diet-induced obese rats. *Calcified Tissue Int*. 2016;98(1):85–93. doi:10.1007/s00223-015-0063-9
98. Wang TH, Li JB, Tian YG, Zheng JX, Li XD, Guo SZ. Association of TNF-α, IGF-1, and IGFBP-1 levels with the severity of osteopenia in mice with nonalcoholic fatty liver disease. *J Orthopaedic Surg Res*. 18(1):915. doi:10.1186/s13018-023-04385-1
99. Yu X, Hu Y, Freire M, Yu P, Kawai T, Han X. Role of toll-like receptor 2 in inflammation and alveolar bone loss in experimental peri-implantitis versus periodontitis. *J Periodontal Res*. 2018;53(1):98–106. doi:10.1111/jre.12492
100. Duda GN, Geissler S, Checa S, Tsitsilonis S, Petersen A, Schmidt-Bleek K. The decisive early phase of bone regeneration. *Nat Rev Rheumatol*. 2023;19(2):78–95. doi:10.1038/s41584-022-00887-0
101. Newman H, Shih YV, Varghese S. Resolution of inflammation in bone regeneration: from understandings to therapeutic applications. *Biomaterials*. 2021;277:121114. doi:10.1016/j.biomaterials.2021.121114
102. Bell KL, Loveridge N, Power J, et al. Structure of the femoral neck in Hip fracture: cortical bone loss in the inferoanterior to superoposterior axis. *J Bone Miner Res*. 1999;14(1):111–119. doi:10.1359/jbmr.1999.14.1.111
103. Okazaki M, Yamada Y, Nishimoto N, Yoshizaki K, Mihara M. Characterization of anti-mouse interleukin-6 receptor antibody. *Immunol Lett*. 84 (3):231–240. doi:10.1016/s0165-2478(02)00202-x
104. Foessl I, Bassett JHD, Bjørnerem Å, et al. Bone phenotyping approaches in human, mice and zebrafish - expert overview of the EU cost action GEMSTONE ("GEnomics of MusculoSkeletal traits TranslatiOnal NEtwork"). *Front Endocrinol*. 2021;12:720728. doi:10.3389/fendo.2021.720728
105. Koh NYY, Miszkiewicz JJ, Fac ML, Wee NKY, Sims NA. preclinical rodent models for human bone disease, including a focus on cortical bone. *Endocr Rev*. 45(4):493–520. doi:10.1210/endrev/bnae004
106. Luo Y, Zhang Q, Shao C, et al. Diagnostic value of LncRNA SNHG16 for osteoporotic fractures and its potential regulation of fracture healing. *Hereditas*. 162(1):54. doi:10.1186/s41065-025-00423-6
107. Wang XF, Zhang YK, Yu ZS, Zhou JL. The role of the serum RANKL/OPG ratio in the healing of intertrochanteric fractures in elderly patients. *Mol Med Reports*. 2013;7(4):1169–1172. doi:10.3892/mmr.2013.1335
108. Metzger CE, Narayanan SA. The role of osteocytes in inflammatory bone loss. *Front Endocrinol*. 2019;10:285. doi:10.3389/fendo.2019.00285
109. Feng W, Liu H, Luo T, et al. Combination of IL-6 and sIL-6R differentially regulate varying levels of RANKL-induced osteoclastogenesis through NF-κB, ERK and JNK signaling pathways. *Sci Rep*. 7:41411. doi:10.1038/srep41411
110. Johnson DE, O'Keefe RA, JR G. Targeting the IL-6/JAK/STAT3 signalling axis in cancer. *Nat Rev Clin Oncol*. 2018;15(4):234–248. doi:10.1038/nrclinonc.2018.8
111. Park J, Zhao Y, Zhang F, et al. IL-6/STAT3 axis dictates the PNPLA3-mediated susceptibility to non-alcoholic fatty liver disease. *J Hepatol*. 2023;78(1):45–56. doi:10.1016/j.jhep.2022.08.022
112. Schmidt-Arras D, Rose-John S. IL-6 pathway in the liver: from physiopathology to therapy. *J Hepatol*. 2016;64(6):1403–1415. doi:10.1016/j.jhep.2016.02.004
113. Sun JY, Du LJ, Shi XR, et al. An IL-6/STAT3/MR/FGF21 axis mediates heart-liver cross-talk after myocardial infarction. *Sci Adv*. 2023;9(14): eade4110. doi:10.1126/sciadv.ade4110
114. McGregor NE, Walker EC, Chan AS, et al. STAT3 hyperactivation due to socs3 deletion in murine osteocytes accentuates responses to exercise- and load-induced bone formation. *J Bone Miner Res*. 2022;37(3):547–558. doi:10.1002/jbmr.4484
115. Sims NA. The JAK1/STAT3/SOCS3 axis in bone development, physiology, and pathology. *Exp Mol Med*. 2020;52(8):1185–1197. doi:10.1038/s12276-020-0445-6
116. Zhu L, Wang Z, Sun X, et al. STAT3/mitophagy axis coordinates macrophage NLRP3 inflammasome activation and inflammatory bone loss. *J Bone Miner Res*. 2022. doi:10.1002/jbmr.4756
117. Latourte A, Cherifi C, Maillet J, et al. Systemic inhibition of IL-6/Stat3 signalling protects against experimental osteoarthritis. *Ann Rheumatic Dis*. 2017;76(4):748–755. doi:10.1136/annrheumdis-2016-209757
118. Palui R, Durgia H, Sahoo J, Naik D, Kamalanathan S. Timing of osteoporosis therapies following fracture: the current status. *Therap Adv Endocrinol Metabolism*. 2022;13:20420188221112904. doi:10.1177/20420188221112904
119. Prystaz K, Kaiser K, Kovtun A, et al. Distinct Effects of IL-6 classic and trans-signaling in bone fracture healing. *Am J Pathol*. 2018;188 (2):474–490. doi:10.1016/j.ajpath.2017.10.011
120. Menger MM, Manuschewski R, Ehnert S, et al. Radiographic, Biomechanical and histological characterization of femoral fracture healing in aged cd-1 mice. *Bioengineering*. 10(2). doi:10.3390/bioengineering10020275
121. Yang X, Ricciardi BF, Hernandez-Soria A, Shi Y, Pleshko CN, Bostrom MP. Callus mineralization and maturation are delayed during fracture healing in interleukin-6 knockout mice. *Bone*. 2007;41(6):928–936. doi:10.1016/j.bone.2007.07.022